

THE FMOS-COSMOS SURVEY OF STAR-FORMING GALAXIES AT $Z \sim 1.6$. IV: EXCITATION STATE AND CHEMICAL ENRICHMENT OF HII REGIONS

D. KASHINO¹, J. D. SILVERMAN², D. SANDERS³, J. S. KARTALTEPE^{4,5}, E. DADDI⁶, A. RENZINI^{7,8}, F. VALENTINO⁶, G. RODIGHIERO⁹, S. JUNEAU⁶, L. J. KEWLEY¹⁰, H. J. ZAHID¹¹, N. ARIMOTO^{12,13}, T. NAGAO¹⁴, J. CHU³, N. SUGIYAMA¹, F. CIVANO^{15,16}, O. ILBERT¹⁷, M. KAJISAWA^{14,18}, O. LE FÉVRE¹⁷, C. MAIER¹⁹, M. ONODERA^{8,12}, A. PUGLISI⁹, Y. TANIGUCHI²⁰, AND COSMOS

Submitted to the Astrophysical Journal

ABSTRACT

We present results on the physical conditions of the interstellar medium of star-forming galaxies at $1.4 \lesssim z \lesssim 1.7$ from the FMOS-COSMOS survey. We use a sample of 701 galaxies, for which the H α emission line is detected, that represents the star-forming population over the stellar mass range $10^{9.6} \lesssim M_*/M_\odot \lesssim 10^{11.6}$ with those at $M_* > 10^{11} M_\odot$ being well sampled. The excitation state and chemical enrichment of the ionized gas are investigated using diagnostic diagrams based on the ratios of emission line strengths, including H α , [NII] λ 6584, [SII] λ 6717,6731, H β , and [OIII] λ 5007. Our data confirm an offset of the star-forming sequence on the BPT diagram ([OIII]/H β vs. [NII]/H α), primarily towards higher [OIII]/H β , compared with local star-forming galaxies. Based on the [SII] ratio, we measure an electron density ($n_e = 222^{+172}_{-128} \text{ cm}^{-3}$), higher than that of local galaxies. Overall, these changes in emission-line properties are due to a higher ionization parameter in high redshift galaxies as demonstrated by a lower than expected [SII]/H α ratio and a comparison to theoretical models. These results likely rule out an offset in the BPT diagram caused by a harder radiation field or AGN as assessed with *Chandra*. Finally, we revisit the mass–metallicity relation by using a conventional [NII]/H α -based indicator and a new calibration based on the [NII]/[SII] ratio introduced by Dopita et al. Consistent with our previous results, the most massive galaxies ($M_* \gtrsim 10^{11} M_\odot$) are fully enriched, while lower mass galaxies have metallicities considerably lower than local galaxies, in agreement with many studies. In addition, we show that the FMOS sample is inconsistent with a “fundamental metallicity relation”, though well-fit with a physically-motivated model of galaxy evolution with gas regulation.

daichi@nagoya-u.jp

¹ Division of Particle and Astrophysical Science, Graduate School of Science, Nagoya University, Nagoya, 464-8602, Japan

² Kavli Institute for the Physics and Mathematics of the Universe (WPI), Todai Institutes for Advanced Study, the University of Tokyo, Kashiwanoha, Kashiwa, 277-8583, Japan

³ Institute for Astronomy, University of Hawaii, 2680 Woodlawn Drive, Honolulu, HI 96822, USA

⁴ National Optical Astronomy Observatory, 950N. Cherry Ave, Tucson AZ 85719, USA

⁵ School of Physics and Astronomy, Rochester Institute of Technology, 84 Lomb Memorial Dr., Rochester, NY 14623, USA

⁶ Laboratoire AIM-Paris-Saclay, CEA/DSM-CNRS-Université Paris Diderot, Irfu/Service d’Astrophysique, CEA-Saclay, Service d’Astrophysique, F-91191 Gif-sur-Yvette, France

⁷ INAF Osservatorio Astronomico di Padova, vicolo dell’Osservatorio 5, I-35122 Padova, Italy

⁸ National Astronomical Observatory of Japan, 2-21-1 Osawa, Mitaka, Tokyo 181-8588, Japan

⁹ Dipartimento di Fisica e Astronomia, Università di Padova, vicolo dell’Osservatorio, 2, I-35122 Padova, Italy

¹⁰ RSAA, Australian National University, Cotter Road, Weston Creek, ACT 2611, Australia

¹¹ Smithsonian Astrophysical Observatory, Harvard-Smithsonian Center for Astrophysics, Cambridge, MA 02138

¹² Subaru Telescope, National Astronomical Observatory of Japan, 650 North A’ohoku Place, Hilo, Hawaii 96720, USA

¹³ Graduate University for Advanced Studies, 2-21-1 Osawa, Mitaka, Tokyo, Japan

¹⁴ Research Center for Space and Cosmic Evolution, Ehime University, Bunkyo-cho, Matsuyama 790-8577, Japan

¹⁵ Yale Center for Astronomy and Astrophysics, 260 Whitney Avenue, New Haven, CT 06520, USA

¹⁶ Harvard-Smithsonian Center for Astrophysics, 60 Garden Street, Cambridge, MA 02138, USA

¹⁷ Aix-Marseille Université, CNRS, LAM (Laboratoire d’Astrophysique de Marseille) UMR 7326, 13388 Marseille, France

¹⁸ Graduate School of Science and Engineering, Ehime University, 2-5

Bunkyo-cho, Matsuyama, Ehime, 790-8577, Japan

¹⁹ University of Vienna, Department of Astrophysics, Tuerkenschanzstrasse 17, 1180 Vienna, Austria

²⁰ The Open University of Japan 2-11 Wakaba, Mihama-ku, Chiba 261-8586 Japan

1. INTRODUCTION

The physical conditions of the interstellar medium (ISM) provide clues to understanding the current state and past activity of star formation and gas reprocessing in galaxies. The study of ionized gas in star-forming (i.e., HII) regions has been carried out through many early observational efforts (e.g., Aller 1942; Pagel et al. 1979, 1980) and the underlying physics has been developed theoretically with photoionization models (e.g., Evans & Dopita 1985; Dopita et al. 2000; Kewley & Dopita 2002). Numerous efforts to study the ISM in low-redshift galaxies ($z \lesssim 0.3$) are based on large spectroscopic data sets such as the Sloan Digital Sky Survey (e.g., Kauffmann et al. 2003b; Tremonti et al. 2004; Brinchmann et al. 2004). A wide range of empirical diagnostics of the gas properties has been established, especially based on spectral features in the rest-frame optical window.

In particular, the Baldwin–Phillips–Terlevich (BPT; Baldwin et al. 1981; Veilleux & Osterbrock 1987) diagnostic diagram compares line ratios $[\text{NII}]/\text{H}\alpha$ and $[\text{OIII}]/\text{H}\beta$ to distinguish star-forming galaxies from those hosting and/or dominated by an active galactic nucleus (AGN). Local star-forming galaxies form a tight “abundance sequence” on the BPT diagram (e.g., Kauffmann et al. 2003b) with line excitation attributed to radiation from young massive stars (type O and B). In contrast, AGNs deviate from this sequence due to harder radiation from an accretion disk. Large data sets such as SDSS have established the precise location of star-forming galaxies and AGNs thus facilitating a relatively clean selection of these populations.

However, the physical conditions of galaxies at higher redshifts ($z \gtrsim 1$), where most key rest-frame optical lines are redshifted into infrared, are still unclear. One would expect the properties of the ionized gas in high- z galaxies to be dissimilar to local galaxies given their higher star-forming activity (for a review, see Madau & Dickinson 2014) and gas fractions (e.g., Genzel et al. 2010; Magdis et al. 2012; Scoville et al. 2014). Over the last decade, the universality of the BPT diagram for high-redshift galaxies has been examined through near-infrared spectroscopic campaigns. Early studies have reported an offset of the distribution of star-forming galaxies at higher redshifts ($z \sim 1\text{--}3$) from the local abundance sequence based on relatively small samples (e.g., Shapley et al. 2005; Erb et al. 2006; Liu et al. 2008). More recent, the offset has been reproduced using larger samples (e.g., Steidel et al. 2014; Shapley et al. 2015; Hayashi et al. 2015) observed with multi-object near-infrared spectrographs. This offset likely reflects more extreme conditions of HII gas in high redshift galaxies such as having a larger ionization parameter (Kewley et al. 2015) or a harder radiation field inferred by their high star formation and/or presence of metal-poor stars (Steidel et al. 2014). Alternative explanations are an enhancement of the nitrogen-to-oxygen abundance and high gas pressure (e.g., Masters et al. 2014). However, such an offset for high-redshift galaxies on the BPT diagram has not firmly been established across the general star-forming population since their location can be significantly affected by sample selection (see Juneau et al. 2014; Shapley et al. 2015).

The gas-phase metallicity (hereafter metallicity) is one of important probes of galaxy evolution as a tool to trace past star formation history. The abundance of elements from nucleosynthesis is further influenced by both inflowing gas that dilutes the metal fraction of the ISM, and outflows that transpose metals into the circumgalactic environment (e.g.,

Köppen & Edmunds 1999; Dalcanton 2007; Ellison et al. 2008; Erb 2008; Finlator & Davé 2008; Mannucci et al. 2010; Cresci et al. 2010; Peeples & Shankar 2011; Bouché et al. 2012; Lilly et al. 2013). In the local universe, a correlation between stellar mass and metallicity has been robustly established based on large data sets such as SDSS (e.g., Tremonti et al. 2004; Andrews & Martini 2013; Zahid et al. 2011). The existence of a mass–metallicity (MZ) relation has been extended up to $z \sim 3$ or more (e.g., Erb et al. 2006; Yabe et al. 2012, 2014, 2015; Zahid et al. 2014a,b) with an evolution where the metallicity decreases with redshift at a fixed stellar mass. We have previously reported an average MZ relation at $z \sim 1.6$ (Zahid et al. 2014b), using a smaller subset of the data from the FMOS-COSMOS program (Silverman et al. 2015), that shows the most massive galaxies as being fully mature at a level similar to local massive galaxies while lower mass galaxies are less enriched as compared to local galaxies. However there still remains some discrepancies between various studies that implement different sample selection methods and/or metallicity determinations.

To further understand the typical characteristics of high- z HII regions, it is highly desirable to construct a well-controlled sample of typical star-forming galaxies at each epoch. With the availability of multi-object near-infrared spectrographs (i.e., MOSFIRE, FMOS, KMOS) on large telescopes, we can access key rest-frame optical emission lines such as $\text{H}\beta$, $[\text{OIII}]\lambda 5007$, $\text{H}\alpha$, $[\text{NII}]\lambda 6584$, and $[\text{SII}]\lambda\lambda 6717, 6731$ for samples consisting of up to 10^3 galaxies at $z \gtrsim 1$ (e.g., Rudie et al. 2012; Tonegawa et al. 2015; Kriek et al. 2015). In this paper, we use a large sample of $\text{H}\alpha$ -detected galaxies that trace the star-forming main sequence over a stellar mass range $10^{9.6} \lesssim M_*/M_\odot \lesssim 10^{11.6}$, from the FMOS-COSMOS survey (Silverman et al. 2015) to study the typical properties of HII regions of galaxies at $1.43 \leq z \leq 1.74$. We use the rest-frame optical key emission lines to evaluate the excitation state, gaseous metallicity, and electron density of HII gas while minimizing the impact of AGNs. This paper is organized as follows. In Section 2, we give an overview of our FMOS-COSMOS survey. Sections 3 and 4 describe our samples and the methods of our spectral analysis. We present our results in Section 5. Section 6 discusses the physical origins of high excitation seen in high- z star-forming galaxies. Section 7 provides an assessment of the effect of AGNs based on our stacking analysis of *Chandra* X-ray images. We present a reanalysis of the metallicity measurements of our sample in Section 8. We finally summarize our results and implications in Section 9. Throughout this paper, we use a cosmology with $(h, \Omega_M, \Omega_\Lambda) = (0.7, 0.3, 0.7)$ and assume the Salpeter (1955) initial mass function (IMF; $0.1\text{--}100 M_\odot$). All magnitudes given in this paper are in the AB magnitude system.

2. OVERVIEW OF THE FMOS-COSMOS SURVEY

The galaxy sample used in this paper is constructed from the data set of the FMOS-COSMOS survey. Here, we provide an overview of the survey, which are extensively described in Kashino et al. (2013) and Silverman et al. (2015).

The FMOS-COSMOS survey is designed to detect $\text{H}\alpha$ and $[\text{NII}]$ from galaxies at $1.43 < z < 1.74$ with the Fiber Multi-Object Spectrograph (FMOS; Kimura et al. 2010) in high-resolution mode ($R \sim 3000$; $1.6\text{--}1.8 \mu\text{m}$). The emission-line sensitivity of the H -long grating with an integration time of five hours is $2 \times 10^{-17} \text{ erg cm}^{-2} \text{ s}^{-1}$ for a 5σ detection. In addition to $\text{H}\alpha$ and $[\text{NII}]$, the $[\text{SII}]\lambda\lambda 6717, 6731$ doublet

can be observed within the H -long window for galaxies with $1.43 < z < 1.67$. At the given spectral resolution, all lines are well separated thus do not suffer from any blending issues. The accuracy of the spectroscopic redshift determination is $\Delta z / (1+z) = 2.2 \times 10^{-4}$ (Silverman et al. 2015). Galaxies with a positive detection of an $H\alpha$ emission line in the H -long spectral window are re-observed with the J -long grating ($1.11\text{--}1.35\ \mu\text{m}$; $R \sim 2200$) to detect $H\beta$ and $[\text{OIII}]\lambda\lambda 5007, 4959$, which are essential to determine the excitation states of the ionized gas in star-forming regions. All of the data are reduced using the FMOS pipeline FIBRE-pac (FMOS Image-Based Reduction Package; Iwamuro et al. 2012).

3. DATA

3.1. Sample selection

In this paper, we utilize a larger catalog of galaxies with spectroscopic redshifts from the FMOS-COSMOS survey than presented in Kashino et al. (2013) and Zahid et al. (2014b). This larger sample is the result of additional FMOS observations carried out between Dec 2013 and Feb 2014 that are not reported in Silverman et al. (2015). The characteristics of this sample are statistically equivalent to those used in the aforementioned papers. Here, we give a brief overview of the construction of our galaxy catalog.

Our sample of galaxies is based on the COSMOS photometric catalog (McCracken et al. 2012; Ilbert et al. 2013) that includes the Ultra-VISTA/VIRCAM photometry and an imposed magnitude limit of $K_S < 23.5$. This K_S -band limit provides a high stellar mass completeness ($\sim 85\%$) of galaxies with $M_* \geq 10^{10} M_\odot$ (Ilbert et al. 2013). The majority of our sample is selected to have a stellar mass above $10^{9.8} M_\odot$ and a photometric redshift between 1.46 and 1.72. These values are derived for each object by fitting the spectral energy distribution (SED) using Le Phare (Arnouts & Ilbert 2011) with population synthesis models (Bruzual & Charlot 2003) and a Chabrier (2003) IMF. Hereafter, we convert all stellar masses to a Salpeter IMF by applying a multiplicative factor of 1.7 (Ilbert et al. 2010).

To achieve a high success rate of detecting the $H\alpha$ emission line, we apply a lower limit of an expected $H\alpha$ flux. The prediction of $H\alpha$ flux represents a total flux from each galaxy (without considering flux loss due to the fiber aperture) calculated with Equation 2 of Kennicutt (1998) based on SFR as derived from the SED fitting, assuming a constant star formation history (see Silverman et al. 2015 for details). Dust extinction is taken into account based on the color excess $E_{\text{star}}(B-V)$, estimated from the SED, and Calzetti et al. (2000) extinction curve. Extinction for the nebular component is related to the stellar extinction via $A(H\alpha) = 3.325 E_{\text{star}}(B-V) / f$, where $f = 0.66$ is assumed. In early pilot observations, a flux threshold of $4 \times 10^{-17} \text{ erg cm}^{-2} \text{ s}^{-1}$ is set without taking into account the $\sim 50\%$ aperture loss. In the subsequent intensive program, the limit of the $H\alpha$ flux was raised to $1 \times 10^{-16} \text{ erg cm}^{-2} \text{ s}^{-1}$. The majority (89%) of our sample have a predicted $H\alpha$ flux higher than $1 \times 10^{-16} \text{ erg cm}^{-2} \text{ s}^{-1}$. This flux limit is equivalent to $\text{SFR} \sim 20 M_\odot \text{ yr}^{-1}$ for galaxies at $z \sim 1.6$.

In this study, we use 701 galaxies (approximately 40% of observed galaxies) having a detection of the $H\alpha$ emission line with a signal-to-noise ratio (S/N) greater than 3 in the H -long spectrum. The range of spectroscopic redshift is $1.43 \leq z \leq 1.74$. We define two subsamples based on the spectral coverage. *Sample-1* consists of all 701 galaxies with a positive $H\alpha$ detection in the H -long band, regardless of the

presence or absence of the J -long coverage. *Sample-2* consists of 310 galaxies (a subset of *Sample-1*) having additional J -long coverage. The numbers of detections of each emission line are summarized in Table 1. For the $[\text{SII}]$ doublet, we count the number of objects with both $[\text{SII}]$ lines detected at either $S/N > 1.5$ or > 3 . The number of galaxies with measurements of their line ratios $[\text{NII}]/H\alpha$, $[\text{SII}]/H\alpha$, $[\text{OIII}]/H\beta$, or a combination of them are provided as well, labeled as N2, S2, O3, and, for example, N2+O3. We further group galaxies by the S/N of their emission line measurements: high-quality (HQ) if $S/N > 5$ for $H\alpha$ and $S/N > 3$ for other lines and low-quality (LQ) if $S/N > 3$ for $H\alpha$ and $S/N > 1.5$ for others.

We make use of mean spectra by stacking in bins of galactic properties (see Section 4.2 for details) to account for galaxies with faint emission lines and avoid a bias induced by galaxies with the strongest lines (i.e., largest SFR and least extinction). For stacking analysis, galaxies are restricted to those having a redshift measurement between $1.43 \leq z \leq 1.67$ to cover all the key emission lines including $[\text{SII}]\lambda\lambda 6717, 6731$. The numbers of galaxies (N_{stack}) used for the stacking analysis are given in the bottom row in Table 1. To check the potential impact of residual OH emission and the suppression mask, we construct a sample that consists of only galaxies for which the redshifted wavelength of $[\text{NII}]\lambda 6584$ is more than 9\AA from an OH line²¹ ($\sim 50\%$ of the full sample) to ensure that the $[\text{NII}]$ line is free from OH contamination (see also Stott et al. 2013). We repeat all analyses throughout this work with this restricted sample and confirm that the results do not change.

3.2. Determination of stellar mass and SFR

Stellar masses and SFRs are derived from SED fitting using Le Phare (Arnouts & Ilbert 2011) with a spectroscopic redshift (measured from FMOS) and a constant star formation history. The statistical properties of the recalculated stellar masses do not differ from the original sample used for target selection. The sample spans a range of stellar mass $9.6 \lesssim \log M_*/M_\odot \lesssim 11.6$ with a median mass of $\log M_*^{\text{med}}/M_\odot = 10.4$. We highlight that our sample includes a large number of very massive galaxies ($M_* \geq 10^{11} M_\odot$; 120 in total, 92 after removing AGN (Section 3.3)).

Figure 1 shows the SFR as a function of M_* for our full sample, compared with the complete distribution of K_S -selected ($K_S < 23.5$) galaxies in the equivalent redshift range ($1.46 \leq z_{\text{photo}} \leq 1.72$, gray dots). The K_S -selected galaxies (7987) show a clear correlation between stellar mass and SFR (i.e., star-forming main sequence) with a standard deviation around the relation of 0.37 dex. Of these, our target galaxies with $M_* \geq 10^{9.8} M_\odot$ and $f_{\text{pre}}(H\alpha) \geq 10^{-16} \text{ erg s}^{-1} \text{ cm}^{-2}$ (2324) are marked as small yellow circles; those with an $H\alpha$ detection (*Sample-1*) are shown as small cyan circles and follow the distribution of the parent sample. To quantify a potential bias in our sample, we fit a power-law relation ($\text{SFR} \propto M_*^\alpha$) to the parent K_S -selected and $H\alpha$ -detected samples separately for galaxies with $M_* \geq 10^{9.8} M_\odot$. While the slope is consistent between the two samples ($\alpha = 0.66 \pm 0.01$ for the former and 0.68 ± 0.02 for the latter), the $H\alpha$ -detected sample is slightly biased towards higher SFRs by ~ 0.15 dex over the entire stellar mass range due to the self-imposed limit on the predicted $H\alpha$ flux. However, such a bias is less than half of the scatter of main sequence. The inset panel shows

²¹ The list of the OH lines in the FMOS coverage is available at <http://www.subarutelescope.org/Observing/Instruments/FMOS/index.html>

TABLE 1
SUMMARY OF EMISSION LINE DETECTIONS OF THE FMOS SAMPLE

Coverage Name	<i>H</i> -long		<i>H</i> & <i>J</i> -long	
	Sample-1	w/o AGNs	Sample-2	w/o AGNs
H α : $S/N > 3$ (5)	701 (500)	642 (469)	310 (241)	283 (224)
[NII]: > 1.5 (3)	436 (278)	383 (233)	216 (133)	190 (110)
[SII]	77 (17)	73 (17)	32 (5)	31 (5)
H β	-	-	138 (99)	127 (94)
[OIII]	-	-	171 (160)	158 (147)
N2: LQ (HQ)	436 (246)	383 (217)	216 (115)	190 (99)
S2	77 (17)	73 (17)	32 (5)	31 (5)
N2+S2	61 (13)	57 (13)	28 (2)	27 (2)
O3	-	-	121 (70)	110 (67)
N2+O3	-	-	87 (40)	76 (37)
S2+O3	-	-	19 (5)	18 (5)
$N_{\text{stack}} (z \leq 1.67)$	-	554	-	246

the normalized distribution of the difference in SFR from the fit to the main sequence for both K_S -selected (filled gray histogram) and H α -detected (blue solid histogram) galaxies. As clearly evident, our final sample traces the star-forming main sequence at $z \sim 1.6$.

We also measure SFRs from the H α flux detected by FMOS following Equation 2 of Kennicutt (1998). As described in Kashino et al. (2013), the observed H α fluxes are corrected for the flux falling outside the FMOS $1''.2$ -diameter fiber. This aperture correction factor is evaluated for each object from a comparison between the observed continuum flux from FMOS spectra and the Ultra-VISTA *H* and *J*-band photometry (McCracken et al. 2012). The H α flux is corrected for dust extinction based on the color excess $E_{\text{star}}(B-V)$, which is estimated from SED-fitting, and a Calzetti et al. (2000) extinction curve, as well as the prediction of H α flux from the SED-based SFRs. While the relation of differential extinction between stellar and nebular components has not some uncertainty at high redshift (Kashino et al. 2013; Price et al. 2014; Koyama et al. 2015; Valentino et al. 2015), we assume a factor $f = E_{\text{neb}}(B-V)/E_{\text{star}}(B-V) = 0.59$, based on a comparison of the predicted and observed H α flux. The application of a different f -factor does not change any of our conclusions.

3.3. AGN removal

AGNs are excluded for a clean investigation of the conditions of HII regions of star-forming galaxies. We identify possible AGNs based on either their X-ray emission, rest-frame optical emission-line width (i.e., H α), or emission-line ratios. From the sample shown in Figure 1, we identify 22 objects (3%) associated with an X-ray point source in the catalog provided by the *Chandra* COSMOS Legacy survey (Civano et al. 2016), which covers the entire FMOS survey area. These X-ray detected galaxies are likely to host AGNs because such luminous X-ray emission ($L_{X\text{-ray}} \gtrsim 4 \times 10^{42} \text{ erg s}^{-1}$ at 0.5–7 keV) is expected to arise from a hot accretion disk. In addition, four objects (less than 1 per cent) have an emission line width (full width at half maximum) greater than 1000 km s^{-1} , usually H α , that are taken to be unobscured (type-I) AGNs; one of these is included in the X-ray point source catalog. We also identify 39 objects (5.5%) based on their rest-frame optical emission-line properties that are located above the BPT classification boundary at $z \sim 1.6$ (Kewley et al. 2013b) (see Section 5.1) or have either a line ratio of $\log[\text{NII}]/\text{H}\alpha > -0.1$ or $\log[\text{OIII}]/\text{H}\beta > 0.9$. Of these, four galaxies are detected in the X-ray band and another object has a broad ($> 1000 \text{ km/s}$) H α line. The majority of AGNs identified based on narrow

line ratios are likely obscured (type-II) AGNs.

In total, 59 (8%) objects are taken as potential AGN candidates, which are marked in Figure 1 (magenta circles). Table 1 lists the number of galaxies in each sample before and after the exclusion of those hosting AGNs. For stacking analysis, we only use galaxies with the AGN candidates having been removed. In Section 7, we address the additional contribution of AGN photoionization to the stacked emission line measurements.

The fraction of the objects with an X-ray detection (3%) is roughly similar to Silverman et al. (2009, 2% at $z \sim 1$), and achieves 10% at $M_* > 10^{11} M_\odot$. Such an X-ray AGN fraction at the high-mass end is lower than those at the equivalent redshift range from the literature ($\sim 30\%$; e.g., Bundy et al. 2008; Brusa et al. 2009; Yamada et al. 2009). This is likely due to the prior selection on the predicted H α flux applied for galaxies in our sample. The total AGN fraction is roughly consistent with Yabe et al. (2014, 6%) that uses a sample of star-forming galaxies at $z \sim 1.4$, while Yabe et al. (2014) do not use any X-ray observations thus probably miss some AGNs. The AGN fraction increases with stellar mass and achieves 25% at $M_* > 10^{11} M_\odot$. Such a trend is consistent with previous studies (e.g., Reddy et al. 2005; Bundy et al. 2008; Brusa et al. 2009).

3.4. Local galaxy sample

We extract a sample of local galaxies from the Sloan Digital Sky Survey (SDSS) Data Release 7 (Abazajian et al. 2009) to compare with the ISM properties of our high- z galaxies. The emission-line flux measurements are from the MPA/JHU catalog (Kauffmann et al. 2003a; Brinchmann et al. 2004; Tremonti et al. 2004) based on Data Release 12 (Alam et al. 2015) for which the stellar absorption is taken into account by subtracting a stellar component as determined from a population synthesis model. We use SFRs from the MPA/JHU catalog that are based on H α luminosities and corrected for aperture loss of the SDSS fibers and extinction based on the Balmer decrement. We convert SFRs to a Salpeter IMF from a Kroupa 2001 IMF by multiplying by a factor of 1.5 (Brinchmann et al. 2004).

Stellar masses are derived with Le Phare (see Zahid et al. 2011 for details) instead of using the JHU/MPA values. Stellar masses from Le Phare are based on a Chabrier IMF and are smaller than those provided by MPA/JHU by approximately 0.2 dex on average with a dispersion between the two estimates of 0.14 dex. For this study, the stellar masses are converted to a Salpeter IMF.

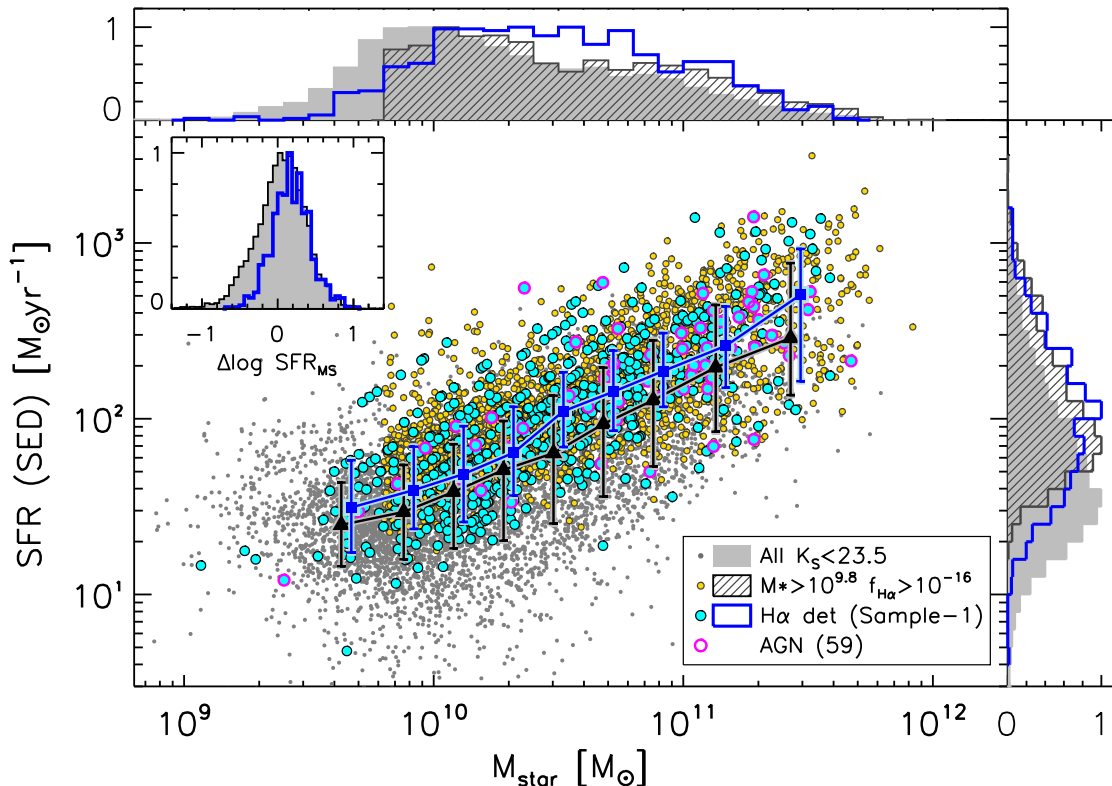


FIG. 1.— SFR (SED) versus M_* for galaxies at $1.43 < z \leq 1.74$. All galaxies with $K_S < 23.5$ and $1.46 \leq z_{\text{photo}} \leq 1.72$ in the FMOS survey area are shown as gray dots and their distribution of stellar mass and SFR are indicated by filled histograms normalized to their peak value. Galaxies with $M_* \geq 10^{9.8} M_\odot$ and a predicted $H\alpha$ flux $f(H\alpha) \geq 1 \times 10^{-16} \text{ erg s}^{-1} \text{ cm}^{-2}$ are shown by yellow circles and hatched histograms. $H\alpha$ -detected galaxies are marked with cyan circles and a thick-line histogram. Potential AGN candidates are marked by magenta circles. The median SFRs in eight stellar mass bins for both the K_S -selected and $H\alpha$ -detected samples are indicated by large symbols (triangles and squares respectively) with error bars indicating the 68 percentiles. The inset panel shows a histogram of the difference in SFR from fit to the main sequence for K_S -selected (filled gray histogram) and $H\alpha$ -detected (thick blue line) galaxies.

The SDSS galaxies are selected over a redshift range of $0.04 < z < 0.1$ to reduce the effects of redshift evolution. Kewley et al. (2005) reported that line measurements are highly biased towards the central area that may be more quenched when a covering fraction is less than 20%. To avoid such aperture effects, we impose a lower redshift limit of 0.04. Furthermore, we require 5σ detections for $H\alpha$ and 3σ for all other emission lines used in this paper ($[\text{NII}]\lambda 6584$, $[\text{SII}]\lambda\lambda 6717, 6731$, $H\beta$, and $[\text{OIII}]\lambda 5007$). We classify galaxies as either star-forming or AGN as those below or above the classification line of Kauffmann et al. (2003b) on the BPT diagram (see Section 5.1). The final sample of local sources consists of 80,003 star-forming galaxies and 31,899 AGNs. In Figure 2, we show the distribution of M_* and SFR for the SDSS star-forming galaxies. For AGNs, the stellar mass distribution is shown by the filled histogram. The central 99 percentiles of the star-forming galaxies and AGNs include objects with $8.7 < \log M_*/M_\odot < 11.1$ and $9.7 < \log M_*/M_\odot < 11.6$, respectively.

4. SPECTRAL ANALYSIS

4.1. Emission line fitting

We perform a fitting procedure that utilizes the MPFIT package for IDL (Markwardt 2009) to measure a flux and an associated error of an emission line on individual and composite spectra. The fitting of key emission lines ($H\alpha$,

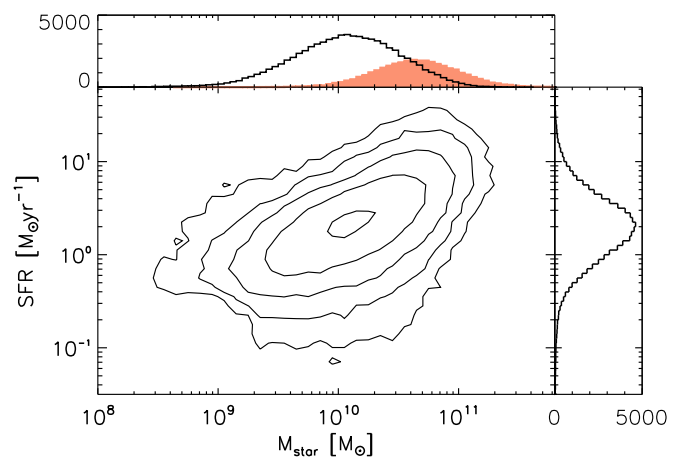


FIG. 2.— M_* vs. SFR for local star-forming galaxies from the SDSS survey. Their distributions of stellar mass and SFR are shown by empty histograms. Filled histogram indicates the stellar mass distribution of local AGNs.

$[\text{NII}]\lambda\lambda 6548, 6584$, $H\beta$, $[\text{OIII}]\lambda\lambda 4959, 5007$) present in individual spectra are described in detail in published papers (Kashino et al. 2013; Silverman et al. 2015). Here, we further perform a fit to the $[\text{SII}]\lambda\lambda 6717, 6731$ lines based on redshift determined from the $H\alpha$ line. For individual spectra, the value of each pixel is weighted by the noise spectra and the pixels

that are impacted by the OH airglow mask are excluded from the fit. For composite spectra, we use weights based on the variance estimated by jackknife resampling (see Section 4.2).

We briefly summarize the steps pertaining to the measurements of the emission line strengths. First, the continuum is fit with a linear function to pixels near the emission lines and subtracted from the data. Each emission line is then modeled with a Gaussian profile. The [NII] and H α lines are simultaneously fit with a single line width. We further fix the ratio [NII] λ 6584/[NII] λ 6548 to the laboratory value of 2.86, and the line widths of [SII] to that of H α . The H β and [OIII] lines are modeled independently from H α + [NII] with the ratio of the [OIII] doublet fixed to 2.98. This avoids any systematic effects potentially due to uncertainties of the wavelength calibration and provides an independent evaluation of key lines (e.g., H α , [OIII]). The observed line widths of H α and [OIII]–H β system agree with each other on average.

4.2. Composite spectra

We construct average spectra to determine the typical strengths of weak lines such as H β , [NII] and [SII]. Individual spectra are stacked in bins of stellar mass. A fair fraction (30%) of the pixels in individual spectra that are strongly impacted by the OH mask and residual sky lines are removed by identifying them in the noise spectra as regions with relatively large errors as compared with the typical noise level of $\sim 5 \times 10^{-19}$ erg cm $^{-2}$ s $^{-1}$ A $^{-1}$ (see Figure 11 in Silverman et al. 2015). We transform all individual spectra to the rest-frame wavelength based on their spectroscopic redshifts. The spectral sampling (0.5 Å/pix) of the co-added spectra corresponds to the pixel resolution of the observed spectra (1.25 Å/pix) at $z = 1.5$.

After subtracting the continuum, the individual deredshifted spectra are averaged by using the *resistant_mean.pro*, an IDL routine available in the Astronomy User’s Library. We apply a 5σ clipping, which removes data that deviates from the median by more than five times the median absolute deviation at each pixel. We do not apply any weighting scheme to avoid possible biases. The associated noise spectra are computed using a jackknife resampling method. The variance at each pixel is given by the following equation

$$\sigma_{\text{jack}}^2 = \frac{N-1}{N} \sum_{i=1}^N \left(F_i - \frac{1}{N} \sum_{i=1}^N F_i \right)^2 \quad (1)$$

where N is the sample size used for stacking (after a 5σ clip) and F_i is the stacked spectra composed of $N-1$ spectra by removing the i -th spectrum. Figure 3 shows the composite spectra of Sample-1 and Sample-2 in five bins of stellar mass. We ensure that the reduced χ^2 of the fit to each composite spectrum is approximately unity (0.8–1.2). Therefore, we conclude that our model fits to the observed composite spectra are accurate. The errors on the flux measurements and flux ratios for the stacked spectra are calculated from Equation 1 with F_i replaced by an arbitrary quantity (i.e., flux or line ratio) measured on the i -th-removed stacked spectrum.

We note that individual spectra are averaged without any renormalization; this may result in a flux-weighted co-added spectrum that is not representative of galaxies with the faintest emission lines. To examine such effects, we generate average spectra by scaling the individual spectra to match the observed amplitude of the H α line for each galaxy. We find that the re-

sults presented in this study do not depend on whether such a scaling is applied or not. All results presented hereafter are based on a stacking analysis without any such renormalization of the individual spectra. Throughout, we measure average emission line ratios using co-added spectra of Sample-1 and Sample-2 split into eight and five bins of stellar mass, respectively. In Table 2, we list the emission line ratios and their associated jackknife errors.

4.3. Correction for Balmer absorption

It is known that the stellar atmospheric absorption is considerable in lowering significantly the observed flux of the H β emission line (e.g., Nakamura et al. 2004; Groves et al. 2012). Therefore, we correct the observed H β flux for this underlying absorption as a function of stellar mass as given in Zahid et al. (2014b):

$$f_{\text{corr}} = \max \left[1, 1.02 + 0.30 \log \left(M_*/10^{10} M_{\odot} \right) \right]. \quad (2)$$

This relation has been converted to be used with a Salpeter IMF. We apply the absorption correction to the measured H β flux of individual galaxies in our FMOS sample, and the measurements based on the composite spectra. The H α flux is not corrected for the stellar absorption since the flux loss is expected to be negligible ($<$ a few percent; see Kashino et al. 2013).

The Balmer absorption correction reduces the line ratio [OIII]/H β by 11% on average and maximally 50% at the high mass end. The typical amount of correction is consistent with Shapley et al. (2015) and Steidel et al. (2014). The application of such a correction does not affect our scientific conclusions. We note that the Balmer absorption correction is applied for only the FMOS sample, and not for the local galaxies from the MPA/JHU catalog, in which the correction is already taken into account by measuring the emission line intensities after the stellar continuum subtraction based on a population synthesis model (see Tremonti et al. (2004) for details).

5. RESULTS

5.1. BPT diagnostic diagram

We present in Figure 4 the BPT diagram for high-redshift galaxies from our FMOS sample. The line ratios for 87 individual galaxies that have detections of all four lines (Sample-2) are indicated by the data points. We further illustrate the quality of the measurements by splitting the sample into two groups: high-quality (HQ, $S/N > 5$ for H α and $S/N > 3$ for [NII] λ 6584, H β , and [OIII] λ 5007) and low-quality (LQ, $S/N > 3$ for H α and $S/N > 1.5$ for others). As previously mentioned, an absorption correction is applied to the observed H β fluxes (see Section 4.3). To aid in our interpretation of the high-redshift data, we plot the distribution of line ratios of local SDSS galaxies (gray contours in Figure 4). We further highlight the local sequence of star-forming galaxies by a commonly used functional form (Kewley et al. 2013a):

$$\log([\text{OIII}]/\text{H}\beta) = \frac{0.61}{\log([\text{NII}]/\text{H}\alpha) + 0.08} + 1.10. \quad (3)$$

More than half of our FMOS galaxies deviates from the above local abundance sequence towards higher [OIII]/H β and/or higher [NII]/H α ratios, and a large number of objects are beyond the local boundary of Kauffmann et al. (2003b), a local demarcation between star-forming galaxies and AGNs. Kewley et al. (2013b) derive a redshift evolution of the boundary to distinguish star-forming galaxies and AGNs. We show

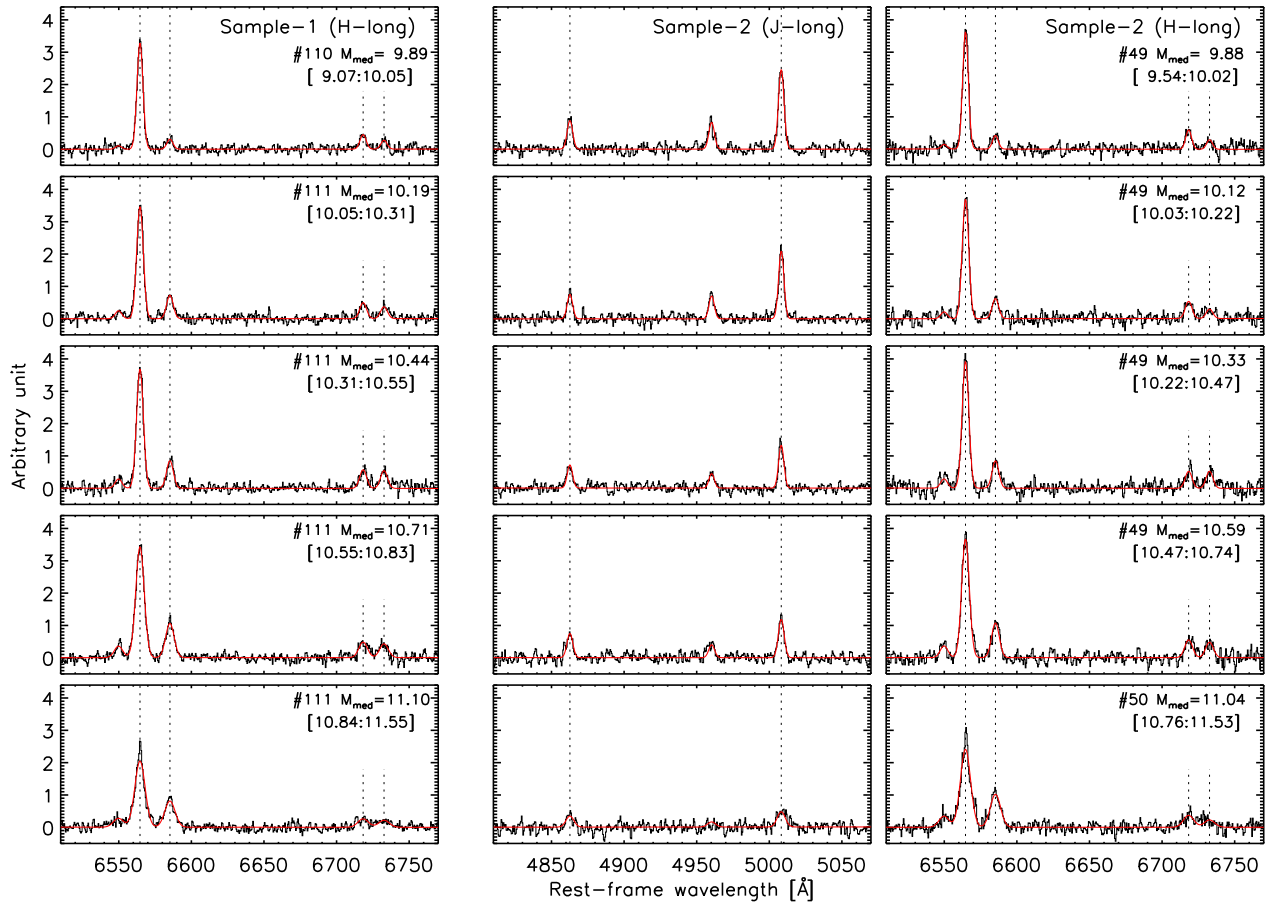


FIG. 3.— Composite spectra in five bins of stellar mass of Sample-1 (left column) and Sample-2 (middle and right column). The number of individual spectra is indicated for each bin (e.g., #110). The stellar mass increases from top to bottom, as their median value ($\log M_*/M_\odot$) and interval are shown in each panel. The observed spectra and the best-fit model are shown by black thin solid lines and red thick curves. The vertical dotted lines show the positions of $H\alpha$, $[\text{NII}]\lambda 6584$, $[\text{SII}]\lambda\lambda 6717, 6731$, $H\beta$, and $[\text{OIII}]\lambda 5007$.

TABLE 2
EMISSION LINE RATIOS

Median M_* ^a	$N2$ ^b	$S2$ ^c	$N2S2$ ^d	$O3$ ^e
Sample-1				
9.84	-1.09 ± 0.12	-0.61 ± 0.07	-0.48 ± 0.13	—
10.04	-0.87 ± 0.07	-0.61 ± 0.07	-0.25 ± 0.09	—
10.21	-0.64 ± 0.04	-0.60 ± 0.06	-0.04 ± 0.07	—
10.35	-0.70 ± 0.05	-0.55 ± 0.05	-0.15 ± 0.07	—
10.51	-0.55 ± 0.04	-0.52 ± 0.06	-0.03 ± 0.06	—
10.69	-0.52 ± 0.04	-0.62 ± 0.07	0.10 ± 0.08	—
10.85	-0.46 ± 0.04	-0.57 ± 0.06	0.12 ± 0.07	—
11.16	-0.37 ± 0.05	-0.61 ± 0.09	0.24 ± 0.10	—
Sample-2				
9.88	-0.93 ± 0.08	-0.60 ± 0.09	-0.34 ± 0.11	0.46 ± 0.06
10.12	-0.77 ± 0.06	-0.64 ± 0.06	-0.13 ± 0.07	0.43 ± 0.06
10.33	-0.67 ± 0.04	-0.56 ± 0.07	-0.11 ± 0.07	0.23 ± 0.07
10.59	-0.53 ± 0.04	-0.54 ± 0.05	0.01 ± 0.05	0.14 ± 0.08
11.04	-0.37 ± 0.04	-0.60 ± 0.07	0.22 ± 0.08	0.03 ± 0.16

^a Median $\log M_*/M_\odot$ of each mass bin.

^b $N2 = \log([\text{NII}]\lambda 6584/H\alpha)$.

^c $S2 = \log([\text{SII}]\lambda\lambda 6717, 6731/H\alpha)$.

^d $N2S2 = \log([\text{NII}]\lambda 6584/[\text{SII}]\lambda\lambda 6717, 6731)$.

^e $O3 = \log([\text{OIII}]\lambda 5007/H\beta)$, corrected for Balmer absorption (see Section 4.3).

this prediction at $z = 1.6$ (thin dotted line) that is consistent with the location of the majority of the FMOS sources. With the same functional form as Equation 3, we perform a fit to our sample and find the following relation at $z \sim 1.6$ (Cyan thick curve in the figure):

$$\log([\text{OIII}]/\text{H}\beta) = \frac{0.61}{\log([\text{NII}]/\text{H}\alpha) + 0.1336} + 1.081. \quad (4)$$

Here, the coefficient is fixed to be the same value (0.61) as the local relation (Equation 3). We remove AGN candidates (see Section 3.3), by using only galaxies with line ratios located in the star-forming region as defined by the redshift-dependent boundary at $z = 1.6$. The mean locus of the FMOS sample seems to be well expressed by this formula. The average measurements, based on the stacked spectra of Sample-2 in five bins of stellar mass (see Table 2), are also representative of the entire trend and in good agreement with the best-fit relation thus confirming a clear offset from the local mean sequence (Kewley et al. 2013a). Here it is important to highlight that our sample maps the distribution on the BPT diagram below $\log([\text{OIII}]/\text{H}\beta) = 0$ down to ~ -0.4 by individual measurement as a result of the considerable sampling rate of the massive galaxy population.

To further examine the robustness of the high- z abundance sequence, we apply a more strict limit on the $[\text{NII}]/\text{H}\alpha$ ratio to remove potential AGNs. Following Valentino et al. (2015), we decrease the N2 limit from -0.1 (see Section 3.3) to -0.4 (Cid Fernandes et al. 2010). With this restricted sample ($N_{\text{stack}} = 225$), we obtain stacked measurements that also show a significant offset from the local mean sequence thus reaffirming our results. We conclude that the offset of the high- z star-forming population cannot be explained by the effects of AGNs.

This offset on the BPT diagram has been previously reported in our FMOS studies (Zahid et al. 2014b; Kartaltepe et al. 2015) and other studies (e.g., Shapley et al. 2005; Erb et al. 2006; Liu et al. 2008; Newman et al. 2014) based on stacking analyses and individual measurements. We show in Figure 4 the fits to the samples at $z \sim 2.3$ from Steidel et al. (2014) (orange dashed line) and Shapley et al. (2015) (magenta long-dashed line). Steidel et al. (2014) derive the relation to rest-frame UV-selected galaxies from the KBSS-MOSFIRE survey, which lies above our relation as a whole. Shapley et al. (2015) also confirm the offset, although more similar to our FMOS sample than the KBSS results. Masters et al. (2014) measured the line ratios for highly active galaxies at $z \sim 2$, whose average measurement is significantly different from the local sequence (Figure 11 in Masters et al. 2014). These differences are likely due to sample selection that results in varying ionization states of each subpopulation.

At $z \sim 1.5$, three groups provide BPT measurements using Subaru/FMOS, including our FMOS-COSMOS program. Yabe et al. (2014) measure line ratios using the stacked spectra of star-forming galaxies at $z \sim 1.4$. The Yabe et al. sample is selected based on stellar mass and $\text{H}\alpha$ flux, and can be considered to be representative of star-forming galaxies at this epoch, whose characteristics are similar to our sample. Their results are well consistent with our stacking measurements on the BPT diagram (see Figure 4 in Yabe et al. 2014). Hayashi et al. (2015) construct a sample of $[\text{OII}]\lambda\lambda 3727, 29$ emitters at $z \sim 1.5$ with an $\text{H}\alpha$ detection with FMOS. Their sample shows larger offset compared to Yabe et al., MOS-DEF, and our samples, while it is consistent with the Stei-

del et al. sample (see Figure 7 in Hayashi et al. 2015). The Hayashi et al. sample follows a M_* -SFR relation with a slope of 0.38, which is shallower than other studies ($\sim 0.7-0.9$, e.g., Kashino et al. 2013; Whitaker et al. 2014). Consequently, the sample is biased towards a population having high specific SFR (sSFR) at $\log(M_*/M_\odot) \sim 9$, and it might be responsible to the observed high $[\text{OIII}]/\text{H}\beta$ ratios (a large BPT offset) in their sample. The authors also mention the possibility that their $[\text{OII}]$ emitter selection causes such a bias.

Based on these independent studies, it is likely that the BPT offset continuously increases with redshift, at least, up to $z \sim 2$. However, it is essential to understand the selection biases to accurately establish the redshift evolution of the location of star-forming galaxies on the BPT diagram. Further investigation on the selection biases and the redshift evolution will be presented in a companion paper (Juneau et al, in preparation). Obviously, the presence of an offset indicates that high- z star-forming galaxies occupy a region in the HII gas parameter space differing from the locus of local galaxies on average. As discussed in Section 6, several possible origins of the offset for high- z galaxies has been suggested and discussed, including ionization parameter, the shape of the UV radiation from the ionizing sources, and gas density (e.g., Masters et al. 2014; Shapley et al. 2015; Hayashi et al. 2015; Kewley et al. 2015).

5.2. Mass-Excitation (MEx) diagram

To further illustrate the magnitude of the $[\text{OIII}]/\text{H}\beta$ offset, we show in Figure 5 the mass-excitation (MEx) diagram (M_* vs. $[\text{OIII}]/\text{H}\beta$). This diagram was introduced by Juneau et al. (2011) to identify galaxies hosting an AGN at intermediate redshifts. Local star-forming galaxies show a decline of the $[\text{OIII}]/\text{H}\beta$ ratio with increasing stellar mass because more massive galaxies are more metal-rich and metal-line cooling becomes more efficient in such systems. In contrast, AGNs present much higher ratios as compared to star-forming population, especially at $M_* \gtrsim 10^{10} M_\odot$.

Figure 5 shows the line ratios $[\text{OIII}]/\text{H}\beta$ as a function of M_* for 121 galaxies in our sample at $z \sim 1.6$ (filled circles), split into two groups: high-quality ($S/N(\text{H}\alpha) > 5$ and $S/N([\text{OIII}], \text{H}\beta) > 3$) and low-quality ($S/N(\text{H}\alpha) > 3$ and $S/N([\text{OIII}], \text{H}\beta) > 1.5$). The distribution of local star-forming galaxies (gray contours) and AGNs (red contours) is indicated for comparison. We highlight the demarcations between star-forming, composite objects, and AGNs, derived by Juneau et al. (2014) for local galaxies (dashed line). It is clear that galaxies in our sample show higher $[\text{OIII}]/\text{H}\beta$ ratios on average as compared to local galaxies at a fixed stellar mass, and that many individual measurements fall within regions classified as composites (between the curves) or AGNs (above upper line) while the error bars are typically too large to constrain the true category for which each one belongs. The average measurements, based on the stacked spectra of Sample-2 in five M_* bins (see Table 2), confirm a substantial offset towards higher $[\text{OIII}]/\text{H}\beta$ ratios by ~ 0.5 dex. Despite the offset, we note that the global trend is similar to local star-forming galaxies, showing a clear negative correlation between stellar mass and line ratio.

Juneau et al. (2014) also derive the offset of the boundary as a function of luminosity threshold of $\text{H}\alpha$ or $[\text{OIII}]\lambda 5007$ emission line (Equation B1 of Juneau et al. 2014) to maximize the fraction of objects successfully classified as either star-forming or AGNs. We shift the boundaries by $\Delta \log M_* = 0.54$ dex (solid lines), assuming an $\text{H}\alpha$ luminos-

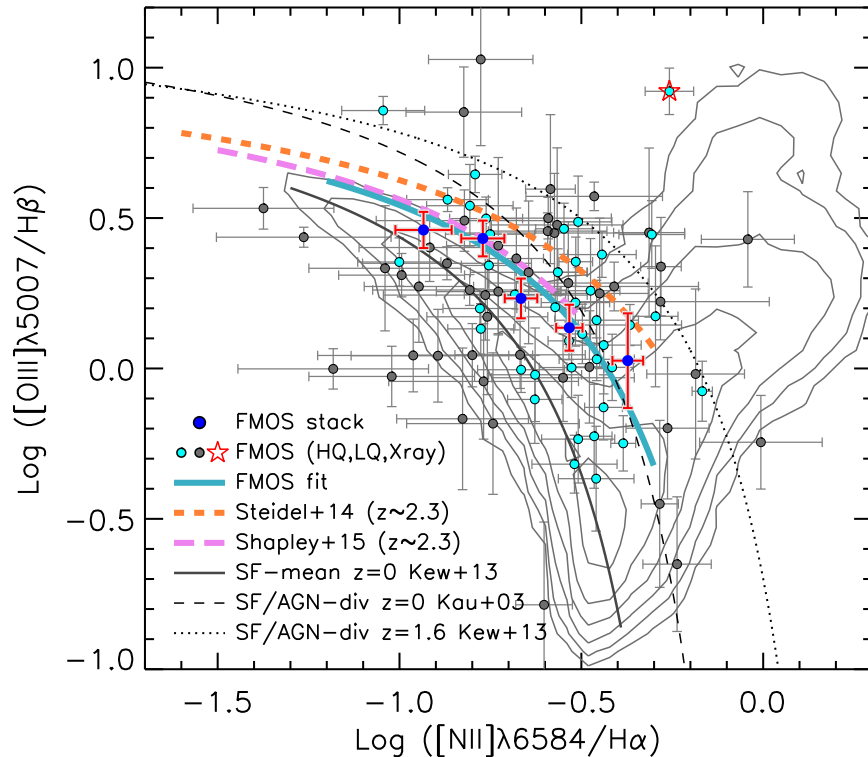


FIG. 4.— The BPT diagnostic diagram: $\log([\text{OIII}]/\text{H}\beta)$ versus $\log([\text{NII}]/\text{H}\alpha)$. Individual FMOS galaxies (87) are shown with circles for two groups: high-quality (HQ, cyan) and low-quality (LQ, dark gray). A single object detected in the X-ray band is indicated by a star. Large blue circles are average measurements (Sample-2) in five mass bin with associated errors. The median stellar mass increases from left to right. Thin curves indicate the empirical mean abundance sequence of local galaxies given by Equation 3 (solid line: Kewley et al. 2013a), the empirical classification of star-forming galaxies and AGNs for the local SDSS sample (dashed line: Kauffmann et al. 2003b), and the empirical prediction of the classification at $z = 1.6$ (dotted line: Kewley et al. 2013b). Thick cyan solid curve is the best fit to our individual measurements (Equation 4). Fits to samples at $z \sim 2.3$ are shown by thick short-dashed (Steidel et al. 2014) and thick long-dashed (Shapley et al. 2015) curves. Contours show the distribution of the local sample in log scale.

ity limit of $L_{\text{H}\alpha} = 10^{42} \text{ erg s}^{-1}$, which corresponds to $\text{SFR} \sim 10 M_{*} \text{ yr}^{-1}$ for our sample. While the amount of the offset is less constrained at high luminosities ($L_{\text{H}\alpha} > 10^{40.7} \text{ erg s}^{-1}$; Juneau et al. 2014), the boundary, derived here, shows a good agreement with galaxies in our FMOS sample. The majority of the FMOS sources fall below the demarcation line thus classified as star-forming galaxies with most of the rest classified as composites. At the same time, half of potential AGNs (star and squares in Figure 5) falls within the AGN-dominant region. While our sample is not purely luminosity-limited, it is likely that the luminosity-dependent boundary derived based on local galaxies provides a good classification even for high redshift galaxies, as originally reported by Juneau et al. (2014). A companion paper further investigates the locus of star-forming galaxies on the BPT and MEx diagrams as a function of emission-line luminosity detection limits (Juneau et al. in preparation).

We also plot the measurements for $z \sim 2.3$ galaxies from Steidel et al. (2014). They show significantly higher line ratios compared to the local galaxies and even to our FMOS sample over the entire stellar mass range probed. These higher $[\text{OIII}]/\text{H}\beta$ ratios are essentially responsible for the large offset on the BPT diagram of the Steidel et al. sample (see Figure 4). These elevated ratios may be due to a combination of sample selection (UV-bright subsample of the population) and the redshift evolution of typical conditions (e.g., an enhanced amount of hotter stars; see Steidel et al. (2014)).

5.3. The $[\text{SII}]\text{-BPT}$ diagram

An alternative BPT diagram compares the line ratios $[\text{SII}]\lambda\lambda 6717, 6731/\text{H}\alpha$ and $[\text{OIII}]\lambda 5007/\text{H}\beta$ to segregate the star-forming population and AGN (hereafter “ $[\text{SII}]\text{-BPT}$ ” diagram; Veilleux & Osterbrock 1987), although it does not provide as clear a separation as that based on $[\text{NII}]/\text{H}\alpha$ (Kewley et al. 2006; Pérez-Montero & Contini 2009). Contrary to offsets seen in the standard BPT diagram at high-redshift (Figure 4), no systematic difference of the $[\text{SII}]\text{-BPT}$ diagram for high-redshift galaxies has been reported (e.g., Domínguez et al. 2013; Masters et al. 2014; Shapley et al. 2015).

In Figure 6, we compare the line ratios $[\text{SII}]/\text{H}\alpha$ and $[\text{OIII}]/\text{H}\beta$ for 19 individual galaxies of Sample-2 (high-quality — $S/N(\text{H}\alpha) > 5$ and $S/N(\text{others}) > 3$; low-quality — $S/N(\text{H}\alpha) > 3$ and $S/N(\text{others}) > 1.5$) and the average line ratios based on stacked spectra in five bins of stellar mass (Table 2). Four objects fall within the AGN region, above the classification line derived by Kewley et al. (2006, thin solid line in Figure 6). One of them is identified as an AGN based on the $[\text{NII}]/\text{H}\alpha$ and $[\text{OIII}]/\text{H}\beta$ ratios (open square), while there is no X-ray detected object here. From the individual measurements, the distribution appears to follow that of local star-forming galaxies; although, we are hampered by the limited sample size and errors on individual measurements. On the other hand, our average measurements clearly indicate a similarity to local galaxies (indicated by the solid curve to rep-

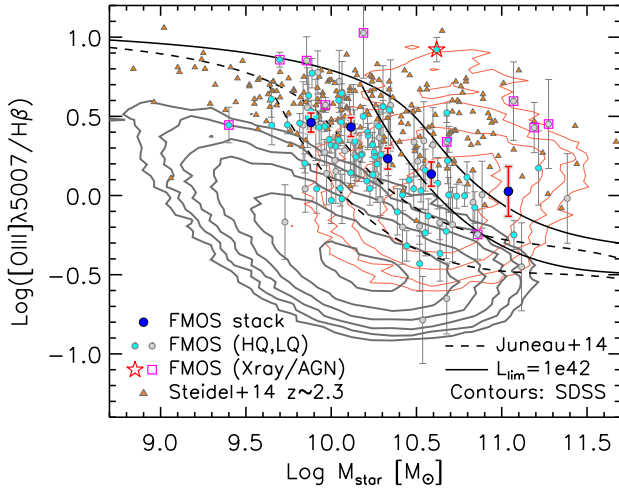


FIG. 5.— The mass-excitation (MEx) diagram: M_* vs. $[\text{OIII}]\lambda 5007/\text{H}\beta$. Individual FMOS galaxies are shown with filled circles for two groups: high-quality (HQ, cyan) and low-quality (LQ, gray). AGN candidates are indicated by a star (X-ray detected source) and magenta squares (others). Large blue circles are average measurements of Sample-2 based on the stacked spectra in five mass bin. Contours show the distributions of the local star-forming galaxies (gray) and AGNs (red). Galaxies in Steidel et al. (2014) at $z \sim 2.3$ are shown with triangles for comparison. Solid and dashed curves indicate demarcations between star-forming, composite objects, and AGNs, derived by Juneau et al. (2014).

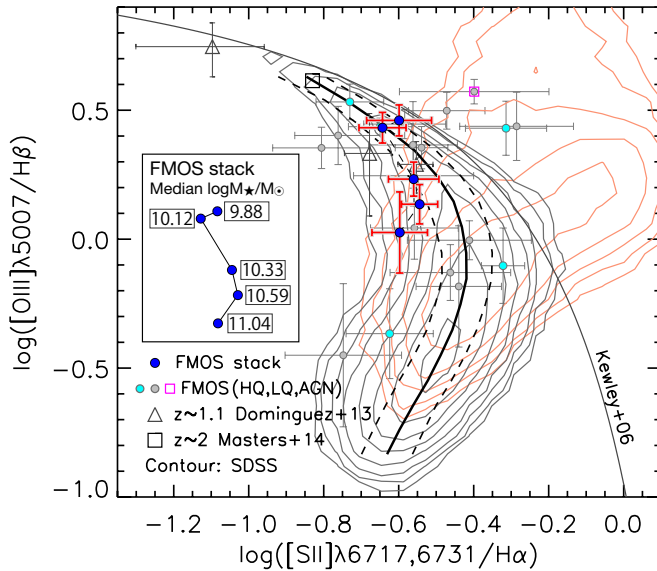


FIG. 6.— [SII]-BPT diagram: $[\text{OIII}]\lambda 5007/\text{H}\beta$ vs. $[\text{SII}]\lambda\lambda 6717, 6731/\text{H}\alpha$. Individual FMOS galaxies are shown with filled circles for two groups: high-quality (HQ, cyan) and low-quality (LQ, gray). A single AGN candidate is indicated by a magenta square. Large blue circles are average measurements in five mass bin (Sample-2) with the median mass of each bin given in the inset box. Data from Domínguez et al. (2013) (triangles) and Masters et al. (2014) (squares) are presented. Contours show the distributions of the local star-forming galaxies (gray) and AGNs (red). Thick solid and dashed curves indicate the median and central 68 percentiles of $\log[\text{SII}]/\text{H}\alpha$ in bins of $\log[\text{OIII}]/\text{H}\beta$ for local star-forming galaxies. Thin solid curve is a demarcation between star-forming galaxies and AGN for local galaxies (Kewley et al. 2006).

resent the median $[\text{SII}]/\text{H}\alpha$ in bins of $[\text{OIII}]/\text{H}\beta$ at the lower masses, while there is a departure towards lower $[\text{SII}]/\text{H}\alpha$ ratios with increasing stellar mass. We further discuss the reasons for such an offset in Section 6.

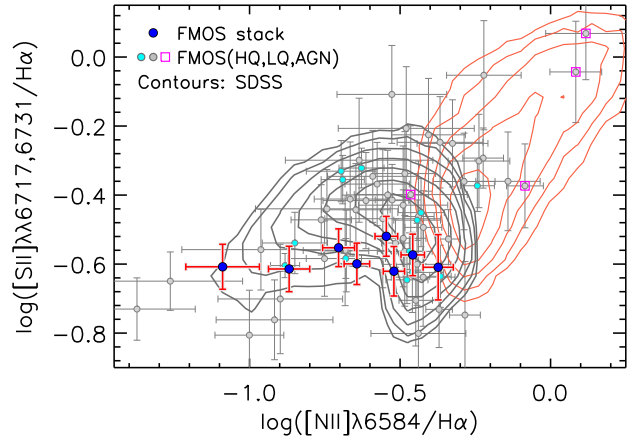


FIG. 7.— Comparison of $[\text{NII}]\lambda 6584/\text{H}\alpha$ and $[\text{SII}]\lambda\lambda 6717, 6731/\text{H}\alpha$. Individual FMOS galaxies are shown with filled circles for two groups: high-quality (HQ, cyan) and low-quality (LQ, gray). Magenta squares indicate AGN candidates. The average measurements are based on the stacked spectra of Sample-1 in eight stellar mass bins (large blue circles). Contours show the distribution of the SDSS star-forming galaxies (gray) and AGNs (red).

An additional diagnostic relation for emission-line galaxies is based on the line ratios $[\text{SII}]\lambda\lambda 6717, 6731/\text{H}\alpha$ and $[\text{NII}]/\text{H}\alpha$ (S2N2 hereafter). This diagram was first introduced by Sabbadin et al. (1977) to distinguish between planetary nebulae, HII regions, and supernova remnants. In past years, this diagram has also been used to separate star-forming galaxies from AGNs (Lamareille et al. 2009; Lara-López et al. 2010a). In Figure 7, we show the S2N2 diagram for 61 individual galaxies (high-quality — $S/N(\text{H}\alpha) > 5$ and $S/N([\text{NII}], [\text{SII}]) > 3$; low-quality — $S/N(\text{H}\alpha) > 3$ and $S/N([\text{NII}], [\text{SII}]) > 1.5$) and average measurements based on stacked spectra (Sample-1; Table 2). Individual galaxies are in general in agreement with the distribution of local star-forming galaxies (gray contours). On the other hand, the average measurements have lower $[\text{SII}]/\text{H}\alpha$ ratios at a given $[\text{NII}]/\text{H}\alpha$ as compared with local galaxies with the exception of those at the highest masses. These average measurements occupy a narrow range of $\log[\text{SII}]/\text{H}\alpha \sim -0.6$ having no specific trend with $[\text{NII}]/\text{H}\alpha$ or stellar mass, as seen with local galaxies, even though our high redshift sample spans a similar range in $[\text{NII}]/\text{H}\alpha$ as local galaxies. Finally, we see that there is minimal contribution of AGNs within our star-forming populations) to our stacked signal while a few individual sources are possibly present.

5.4. Electron density

The electron density n_e can be measured from the intensity ratio $[\text{SII}]\lambda 6717/[\text{SII}]\lambda 6731$. Here, we convert the [SII] doublet ratio into n_e using the TEMDEN routine from the NEBULAR package of STSDAS/IRAF, assuming a fixed electron temperature of $T_e = 10^4$ K. While this temperature is commonly assumed for typical HII regions, the electron temperature is sensitive to the gas-phase metallicity with a variation of $\sim 5000\text{--}20000$ K (e.g., Wink et al. 1983; Andrews & Martini 2013). We note that the dependence of the electron density, derived from [SII] lines, on temperature is weak around this choice (maximally $\lesssim 0.2$ dex; Copetti et al. 2000). The line ratio is sensitive to the electron density over the range $10 \lesssim n_e/\text{cm}^3 \lesssim 5 \times 10^3$, while it

saturates at upper ($[\text{SII}]\lambda 6717/[\text{SII}]\lambda 6731 \sim 1.45$) and lower (~ 0.45) limits for lower and higher electron densities, respectively. The doublet lines are well resolved with the high-resolution of FMOS (see Figure 3). Due to the close spacing of the lines in wavelength, the measurements are free from uncertainties in the absolute flux calibration and not impacted by dust extinction. However, no single galaxy has a significant measurement of the line ratio to constrain the electron density. Therefore, we rely on stacking analysis.

In Figure 8, we present the average ratio $[\text{SII}]\lambda 6717/[\text{SII}]\lambda 6731$ based on stacked spectra (Sample-1). The average electron density of the full sample is $n_e = 222^{+172}_{-128} \text{ cm}^{-3}$ with errors based on jackknife resampling. This value is higher than the average electron density in local galaxies ($n_e = 10\text{--}100 \text{ cm}^{-3}$; Brinchmann et al. 2008). We split the sample into mass bins, but do not find any significant trend with mass due to large uncertainties on our measurements.

Our results are consistent with findings reported in the literature. For example, Shirazi et al. (2014) find that the electron density of ionized gas in high- z star-forming galaxies ($z \approx 2.4\text{--}3.7$) is enhanced as compared to matched local galaxies, selected to have the same stellar mass and sSFR. Shimakawa et al. (2015) estimated the electron densities of 14 $\text{H}\alpha$ emitters at $z = 2.5$ by the line ratio $[\text{OII}]\lambda 3729/\lambda 3726$, and find a median electron density of 291 cm^{-3} . Sanders et al. (2016) found a median $n_e = 225^{+119}_{-4} \text{ cm}^{-3}$ from the $[\text{OII}]$ doublet and $n_e = 290^{+88}_{-169} \text{ cm}^{-3}$ from the $[\text{SII}]$ doublet for a sample at $z \sim 2.3$ from the MOSDEF survey. Onodera et al. (2016) found $\sim 10^{2-3} \text{ cm}^{-3}$ for star-forming galaxies at $z \approx 3.3$. Therefore, we can safely conclude that HII regions in high- z galaxies do have an electron density a few to several times larger than that of local galaxies on average.

Moreover, we compare our measurement with local galaxies having high SFRs that match those of our FMOS sample. We select local star-forming galaxies with $\Delta \log \text{SFR} > 0.7$ dex, where $\Delta \log \text{SFR}$ is defined as the difference between the observed SFR and the typical value of main-sequence galaxies at a given stellar mass (Elbaz et al. 2007). Figure 8 shows that such high-SFR local galaxies are biased towards a smaller $[\text{SII}]$ doublet ratio (i.e., a higher electron density) that is more similar to that of our high- z sample, as compared to the entire local sample.

5.5. The line ratio $[\text{NII}]/[\text{SII}]$

Kewley & Dopita (2002) investigated the usability of the line ratio $[\text{NII}]\lambda 6584/[\text{SII}]\lambda \lambda 6717, 6731$ as an abundance diagnostic. Sulphur is one of α -elements, including e.g., O, Ne, Si, produced through *primary* nucleosynthesis in massive stars and supplied to the ISM through type-II supernovae. In contrast, nitrogen is generated through the primary origin and the *secondary* process that uses heavy elements initially stored in stars, such as the CNO cycle, in which ^{12}C and ^{16}O are converted into ^{14}N . The production of the secondary nitrogen increases with the increasing amount of initially-contained metals in stars. Therefore, the $[\text{NII}]/[\text{SII}]$ ratio is sensitive to the total chemical abundance at a regime where the secondary nitrogen production is predominant, while it is almost constant when most of nitrogen has a primary origin (see e.g., Figure 4 of Kewley & Dopita 2002). While the values of $[\text{NII}]/\text{H}\alpha$ and $[\text{SII}]/\text{H}\alpha$ depend on the ionization parameter, the behavior of $[\text{NII}]$ and $[\text{SII}]$ track each other. In particular, the $[\text{NII}]/[\text{SII}]$ ratio is not so sensitive to changes

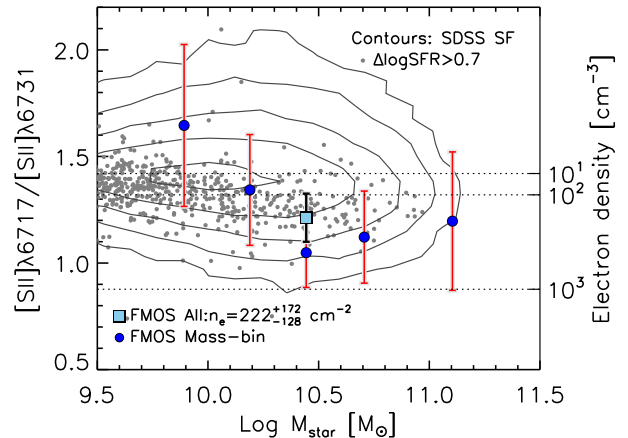


FIG. 8.— The line ratio of $[\text{SII}]\lambda 6717/[\text{SII}]\lambda 6731$ as a function of stellar mass. Blue filled circles indicate the average measurements based on the stacked spectra in five bins of stellar mass (Sample-1), and the cyan square shows the measurement based on the stacked spectrum of the entire sample. Contours show the distribution of the local star-forming galaxies with small gray circles highlighting those with $\Delta \log(\text{SFR}) \geq 0.7$. The corresponding electron densities are given on the right vertical axis and by the horizontal dashed lines ($n_e = 10, 10^2$ and 10^3 cm^{-3}).

in the ionization parameter q for $\log(q/\text{cm s}^{-1}) \gtrsim 7.5$. (see e.g., Figure 20 of Dopita et al. 2013). Such a level for the ionization parameter is expected for high- z star-forming galaxies (e.g., Nakajima & Ouchi 2014). The advantage of the use of $[\text{NII}]/[\text{SII}]$ is that their wavelengths are separated by only $\sim 140 \text{ \AA}$, hence they are able to be observed simultaneously and the line ratio is nearly free from the effect of dust extinction (typically < 0.03 dex). Here we do not take account for the dust extinction, and define

$$N2S2 = \log([\text{NII}]\lambda 6584/[\text{SII}]\lambda \lambda 6717, 6731), \quad (5)$$

In Figure 9a, we show the $[\text{NII}]/[\text{SII}]$ ratio as a function of stellar mass for local star-forming galaxies (contours) and our FMOS sample (filled circles). The local sample shows a clear correlation between the line ratio and stellar mass above $M_* \sim 10^{9.5} M_\odot$ and reaches $N2S2 \sim 0.3$ at the massive end ($\gtrsim 10^{11} M_\odot$), while the line ratio is almost constant ($N2S2 \sim -0.4$) below $\sim 10^{9.2} M_\odot$. These two trends correspond to the regimes where either the primary or secondary origin of nitrogen production is dominant. We find that 61 individual galaxies with a $N2S2$ measurement show a significant correlation with stellar mass at $> 99\%$ confidence level. The trend of these individual measurements are well represented by the average measurements based on the composite spectra of Sample-1 in eight bins of stellar mass (see Table 2). The average $N2S2$ ratio of our sample spans $\sim -0.5\text{--}0.3$ with a strong correlation with stellar mass. This indicates that, on average, the secondary nitrogen production is more predominant in more massive galaxies, and also, for the majority of our sample, the ISM is sufficiently enriched enough that nitrogen is predominantly produced by the secondary process. In contrast, it is interesting to highlight that the primary nitrogen production is still likely predominant in the lowest massive galaxies in our sample ($M_* \lesssim 10^{10} M_\odot$). The $N2S2$ reaches to the same level as local galaxies at the massive end ($\gtrsim 10^{11} M_\odot$) while, on average, galaxies with $M_* < 10^{11} M_\odot$ have lower $N2S2$ values than found in local galaxies at the same stellar mass. That is to say, in such galaxies, the intrinsic

sic nucleosynthesis has not proceeded as much as local galaxies. Obviously, this trend is related to the mass–metallicity relation as discussed in Section 8.

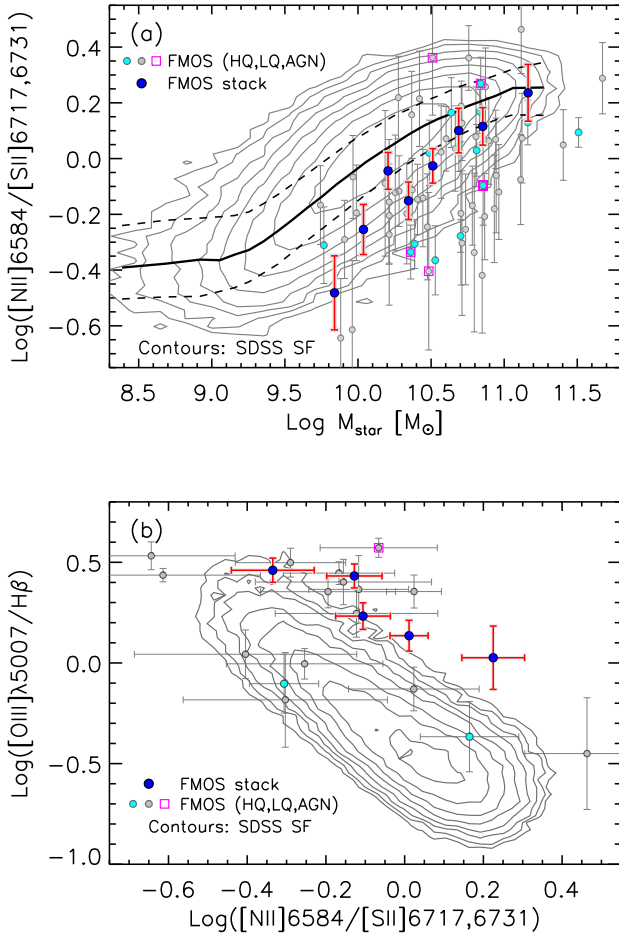


FIG. 9.— *Panel (a)*: The line ratio of $[\text{NII}]\lambda 6584/[\text{SII}]\lambda\lambda 6717, 6731$ ($N2S2$) as a function of stellar mass. Symbols are the same as Figure 7. A solid line represents the median $N2$ value in small bins of stellar mass and dashed lines indicate the interval containing the central 68% of the local galaxies. *Panel (b)*: Comparison of the line ratios of $[\text{NII}]\lambda 6584/[\text{SII}]\lambda\lambda 6717, 6731$ and $[\text{OIII}]\lambda 5007/H\beta$. Individual FMOS galaxies are shown with filled circles for two groups: high-quality (HQ, cyan) and low-quality (LQ, gray). Magenta square indicates an AGN candidate. The average measurements are based on the stacked spectra of Sample-2 in five stellar mass bins (large blue circles). The stellar mass increases from the left to right.

Figure 9b compares the line ratios $[\text{OIII}]/H\beta$ and $[\text{NII}]/[\text{SII}]$. The individual measurements (17 objects; high-quality — $S/N(H\alpha) > 5$ and $S/N(\text{others}) > 3$; low-quality — $S/N(H\alpha) > 3$ and $S/N(\text{others}) > 1.5$) are roughly consistent with the distribution of local star-forming galaxies. In contrast, the average measurements, based on the Sample-2 composite spectra in five mass bins, clearly show higher $[\text{OIII}]/H\beta$ ratios at a given $[\text{NII}]/[\text{SII}]$ (and *vice versa*) as compared to local galaxies. This characteristic of high- z star-forming galaxies is very similar to that found in the MOSDEF sample at $z \sim 2.3$ using the individual measurements (see Figure 8 in Shapley et al. 2015). This fact qualitatively indicates that high- z star-forming galaxies tend to maintain higher excitation state relative to their evolutionary stage of chemical

enrichment, than local galaxies at a similar level of chemical enrichment.

6. PHYSICAL EXPLANATION FOR THE BPT OFFSET

To understand the characteristics of the HII regions of high- z star-forming galaxies, it is essential to specify the primary cause of the offset seen in the BPT diagram, which has been reported by many studies (e.g., Shapley et al. 2005; Erb et al. 2006; Liu et al. 2008; Newman et al. 2014; Masters et al. 2014; Zahid et al. 2014b; Yabe et al. 2014; Steidel et al. 2014; Kartaltepe et al. 2015; Hayashi et al. 2015). Several possible factors have been suggested and discussed, including ionization parameter, hardness of the EUV radiation field, and gas density (pressure). Kewley et al. (2013a) summarize the effects of varying ISM properties on the star-forming locus in the BPT diagram: a larger gas density and a harder ionizing radiation could cause an offset towards both higher $[\text{NII}]/H\alpha$ and higher $[\text{OIII}]/H\beta$ and larger ionization parameter enhances $[\text{OIII}]/H\beta$ especially. Recently, an elevation of nitrogen-to-oxygen (N/O) abundance ratio has been suggested as an origin of the offset (e.g., Masters et al. 2014; Shapley et al. 2015).

The MEx diagram (Figure 5) indicates that galaxies in our sample have elevated $[\text{OIII}]/H\beta$ line ratios compared with local galaxies over the full stellar mass range ($10^{9.6} \lesssim M_*/M_\odot \lesssim 10^{11.6}$), sampled by our survey. The $[\text{OIII}]/H\beta$ ratio is known to become lower as O/H increases in the high metallicity regime where the ionized gas temperature decreases. We would expect to see the offset in $[\text{OIII}]/H\beta$ decrease with stellar mass since the most massive galaxies in our sample are already fully enriched whereas a large offset is still apparent for galaxies with $M_* \gtrsim 10^{11} M_\odot$. Higher $[\text{OIII}]/H\beta$ ratios are also seen at a given stage of chemical enrichment as indicated by the $[\text{NII}]/[\text{SII}]$ ratio (see Figure 9b). While ionization due to AGN may be present, we consider such an additional ionization mechanism in Section 7 and find it is likely negligible, at least not enough to fully explain the offset.

Based on our observations, we further investigate the hypothesis that the higher $[\text{OIII}]/H\beta$ ratios are the result of a higher ionization parameter as compared to local galaxies. With the higher gas density of our sample (Section 5.4), a higher ionization parameter requires an increase in the production rate of ionizing photons, caused by either a scaling up or a hardening of the ionizing radiation field. The former case could be expected to occur when a larger number of stars form in individual HII regions as compared with local galaxies (Kewley et al. 2015). The latter case may be due to a top-heavy IMF that increases the relative amount of hot massive stars, or a metal-poor stellar population that will have a harder spectrum (see e.g., Levesque et al. 2010).

We can use the $[\text{SII}]/H\alpha$ ratio as an indicator of ionization parameter and hardness of the ionizing radiation field. A higher ionization parameter increases the excitation of $S^+ \rightarrow S^{++}$ that decreases the $[\text{SII}]/H\alpha$ ratio. Because our data show $[\text{SII}]/H\alpha$ ratios, suppressed as compared to local galaxies at a given level of excitation, which is probed by the $[\text{OIII}]/H\beta$ ratio (see Figure 6), it is likely that the offset on the BPT diagram for typical high- z star-forming galaxies is caused primarily by an increase in the ionization parameter. Furthermore, the $[\text{SII}]/H\alpha$ ratio increases sensitively for a harder ionizing radiation field since the ionization of neutral sulphur atoms is enhanced (Levesque et al. 2010). This implies that the enhancement of the ionization parameter is caused by a

scaling up of the total radiation field and that a harder ionizing radiation field is less likely as a predominant origin of the BPT offset. This has been achieved by the finding of an offset on the [SII]-BPT diagram (Figure 6), which is obtained by mapping the diagram down to $\log([\text{OIII}]/\text{H}\beta) \sim 0$ (i.e., the vertical regime of the sequence) with our high sampling rate of massive galaxies. Here, we note that the [SII]/H α ratio increases with metallicity. As shown in Figure 9b, our $z \sim 1.6$ sample likely has a larger metal abundance as compared to local galaxies at a fixed [OIII]/H β ; nevertheless the [SII]/H α ratio is suppressed relative to local galaxies. Therefore, we conclude that the suppression in [SII]/H α is caused by a large ionization parameter, as described above.

Furthermore, we evaluate the ionization parameter of our sample based on a theoretical model. Recently, Dopita et al. (2016) proposed a diagnostic with combinations of the line ratios [NII] λ 6584/H α , [NII] λ 6584/[SII] λ λ 6717,6731, and [OIII] λ 5007/H β to clearly separate a dependence on the metallicity from the effects of ionization parameter and gas pressure (see Figure 2 in Dopita et al. (2016)). In Figure 10, we show our data, based on stacked spectra in five mass bins (Sample-2), with the theoretical grids of MAPPINGS V (Dopita et al. 2016) overlaid. The model values are computed as a function of ionization parameter and metallicity, for different gas pressure. Here the ionization parameter, $U = q/c$, is defined as the ratio of ionizing photon flux to the hydrogen atom density (divided by speed-of-light c) at the inner surface of ionized clouds. Based on the theoretical models, the average measurements for our FMOS sample (filled circles in Figure 10) vary with metallicity (y -axis) and the ionization parameter is almost independent of stellar mass. Given $\log P/k \sim 6.2$ – 6.7 for our sample (suggested by the electron density estimated from the [SII] ratio), our sample has ionization parameters $\log U \sim -3.3$ – -3.2 , approximately 0.3 dex higher on average than the average of local star-forming galaxies ($\log U \sim -3.5$). Our results are consistent with previous studies showing that typical high- z ($0.5 \lesssim z \lesssim 3$) galaxies have an ionization parameter enhanced by a factor of ~ 2 – 10 compared with local galaxies (e.g., Shirazi et al. 2014; Nakajima & Ouchi 2014; Hayashi et al. 2015; Onodera et al. 2016). We use the y -axis value to evaluate the metallicity in Section 8.2.

A higher HII gas density increases both [OIII]/H β and [NII]/H α ratios by enhancing the collisional excitation of O $^{++}$ and N $^+$. As a result, the global enhancement of the gas density expects to move the entire abundance sequence towards the upper-right side on the BPT diagram (e.g., Kewley et al. 2013a). Brinchmann et al. (2008) found that SDSS galaxies with a larger n_e tend to lie above the mean abundance sequence. However, high electron density, by itself, does not fully explain the offset on the BPT diagram and lower ratio of [SII]/H α . Rather, a sufficient high ionizing photon flux from the ionizing source is necessary to produce both a large ionization parameter and higher gas density at the inner surface of HII gas clouds if a fixed inner radius is assumed because the ionization parameter is inversely proportional to the gas density. Therefore, we argue that a high ionization parameter likely characterizes the properties of our sample, supposed by the lower [SII]/H α ratios and the comparison using the theoretical model (Figure 10), and that an increase of ionizing photon flux is desirable for individual HII regions. In contrast, a harder ionizing radiation field or AGN are unlikely the primary cause of the BPT offset in high- z galaxies.

Previous studies have reported a lack of any significant

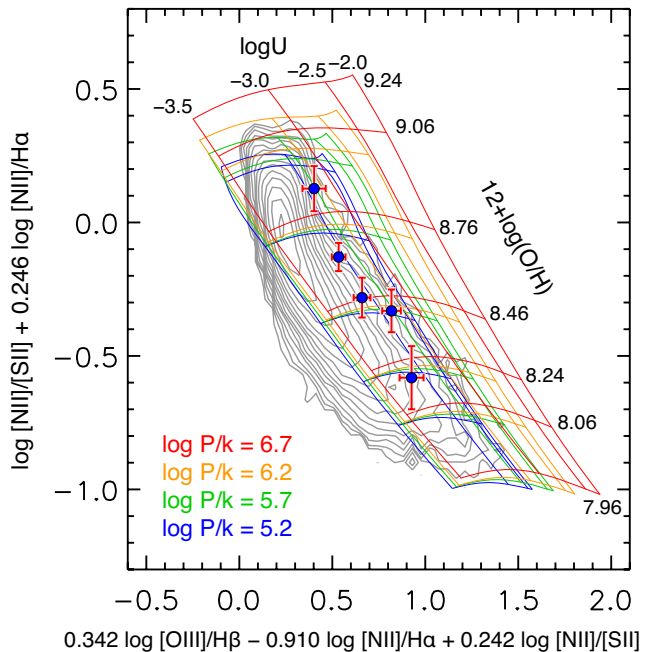


FIG. 10.— Comparison of combinations of line ratios ([NII] λ 6584/H α , [NII] λ 6584/[SII] λ λ 6717,6731, and [OIII] λ 5007/H β). The average measurements are based on the stacked spectra of Sample-2 in five stellar mass bins (large blue circles). The stellar mass increases from the bottom to top. Contours show local star-forming galaxies. Grids show model predictions for different ISM conditions (from Figure 2 of Dopita et al. 2016): metallicity, ionization parameter (U), and gas pressure (P).

offset between local and high- z galaxies on the [SII]-BPT diagram. Those studies have motivated us to consider an origin of the offset on the BPT diagram that is not directly related to the excitation state. Recently, an elevated nitrogen-to-oxygen (N/O) abundance ratio at a given O/H has been suggested as such a possible cause of the BPT offset towards large [NII]/H α at a fixed [OIII]/H β (e.g., Masters et al. 2014; Steidel et al. 2014; Shapley et al. 2015; Yabe et al. 2015; Sanders et al. 2016). For local HII regions in nearby galaxies, the N/O ratios have been measured as a function of O/H (van Zee et al. 1998; Pilyugin et al. 2012), that show a constant value of $\log(\text{N/O}) \approx -1.5$ and an increase of up to $\log(\text{N/O}) \approx -0.3$ above $12 + \log(\text{O/H}) \sim 8.1$ – 8.5 . Assuming the abundance ratio of the two α -elements, oxygen and sulphur, to be nearly constant, the line ratio [NII]/[SII] is expected to be an indicator of the N/O abundance ratio (e.g., Shapley et al. 2015; Yabe et al. 2015; Hayashi et al. 2015). According to a relation derived by Pérez-Montero & Contini (2009), our sample spans a range of the N/O ratio from $\log(\text{N/O}) = -1.5$ to -0.4 . However, the quantitative constraint of N/O–O/H calibration absolutely requires a metallicity determination that is independent of N abundance (e.g., direct T_e or R_{23} index) and a reliable calibration between [NII]/[SII] and N/O in realistic conditions of high- z galaxies. While our existing data cannot solve these problems, future [OII] λ λ 3726,3729 follow-up observations are expected to shed light on these issues.

7. ASSESSMENT OF AGN CONTAMINATION

As described in Section 3.3, we remove AGNs from our star-forming galaxy samples for all analyses in this paper. Our data, as presented on line-ratio diagrams (Figures 4, 6 and 7), shows no strong signature of ionizing radiation from AGN. However, the possibility that weak and/or obscured AGNs

affect the results cannot be completely ruled out. Here, we assess the contribution of such hidden AGNs on the results based on the co-added spectra.

X-ray emission is an effective indicator of the existence of an AGN. We measure the average X-ray luminosities by stacking the *Chandra X-ray Observatory/Advanced CCD Imaging Spectrometer (ACIS)-I* images from the *Chandra-COSMOS Legacy survey* (Elvis et al. 2009; Civano et al. 2016) by using the *CSTACK* tool²² (v4.3; Miyaji et al. 2008). To examine how the X-ray luminosity depends on the exclusion of individually-detected AGN, we compare three samples with different criteria of the removal of possible AGNs; 1) no AGN cut is applied, 2) excluding individual X-ray detected sources, and 3) excluding all possible AGN candidates (X-ray sources, $\text{FWHM}(\text{H}\alpha) > 1000 \text{ km s}^{-1}$, or identified with the BPT diagram; see Section 3.3). The last case is implemented for the results based on stacking analysis throughout the paper. Figure 11 shows the stacked X-ray images, separately in two bandpasses (soft: 0.5–2 keV, hard: 2–8 keV), from the two samples without (case 1) and with (case 3) AGN removal. We combine the images in five bins of stellar mass. Therefore, we have no X-ray image for the $\sim 10\%$ of objects in our sample, which are not considered for the X-ray stacking analysis.

The average count rate is converted into flux assuming a spectrum with $\Gamma = 1.7$ and a Galactic column density $N_{\text{H}} = 2.7 \times 10^{20} \text{ cm}^{-2}$ (Elvis et al. 2009; Dickey & Lockman 1990). The average rest-frame X-ray luminosity is calculated as Equation 4 in Lehmer et al. (2008), with a median redshift. Table 3 lists the X-ray luminosities and associated errors in each bin. When no AGN cut is applied (case 1), the X-ray emission is significantly detected in the two most massive bins at $S/N > 5$ in both the soft and hard bandpasses. When the AGN cut is applied (case 2 and 3), only the most massive bin ($\log M_*/M_{\odot} > 11.1$) presents a significant detection ($S/N > 3$) in the X-ray band. In the third and fourth bins ($10.4 < \log M_*/M_{\odot} < 11.1$), the X-ray emission is detected at a significance of $S/N \sim 2-3$. There are cases with no detection ($S/N < 1$) in the lowest two mass bins, in which there is no or a few objects that are individually detected in the X-ray band (see Table 3).

To further investigate the presence of AGN, we compare the mean SFR and mean X-ray luminosity of the full *Chandra* bandpass ($L_{0.5-8 \text{ keV}}$) in each bin in Figure 12. The mean SFRs are derived from dust-corrected $\text{H}\alpha$ luminosity (see Section 3.2). Following Lehmer et al. (2008), we compare our data with an $\text{SFR}-L_{\text{X-ray}}$ relation for star-forming galaxies derived by Persic & Rephaeli (2007) and a relation with three times large X-ray luminosity, which is used to distinguish AGNs from non-AGN. We compare the measurements for the samples with the different X-ray exclusion criteria (cases 1, 2, and 3). We see that $L_{0.5-8 \text{ keV}}$ is correlated with SFR at $\text{SFR} \gtrsim 100 M_{\odot} \text{ yr}^{-1}$ ($M_* \gtrsim 10^{10.4} M_{\odot}$) in all the cases and that the removal of individual X-ray detected sources primarily affects the average X-ray luminosity of the more massive bins. As a result of the AGN exclusion, the X-ray luminosities are reduced down to the level where the residual contribution from AGNs likely to be negligible in three larger stellar mass bins. For two lower mass bins, upper limits on $L_{0.5-8 \text{ keV}}$ are calculated as 1.5 times the noise level shown by the downward arrows.

Figure 12 indicates that, once the individually detected

AGNs are removed, the contribution to the X-ray luminosities in the stack from unidentified AGNs is small, and that levels of the residual X-ray luminosity are comparable to the levels that are normally expected for star-forming galaxies (solid line in Figure 12). While the limit of the lowest mass bin does not reject a probability that a contribution from AGNs exists, the AGN contribution can be expected to be negligible in such a range of stellar mass. Therefore, we conclude that the impact from AGN are small in our stacking analysis enough to appropriately assess the properties of star-forming HII regions over the entire stellar mass range spanned by our sample.

8. REVISITING THE MASS–METALLICITY RELATION

We previously reported the metallicity measurements of individual galaxies and the average mass–metallicity (MZ) relation based on our FMOS program (Zahid et al. 2014b) using a smaller subset (162 galaxies) of the current data set with an sBzK selection (Daddi et al. 2004). Our MZ relation indicated that the most massive galaxies at $z \sim 1.6$ are fully mature similar to local massive galaxies while the lower mass galaxies are less enriched as compared to local galaxies at a fixed stellar mass. The difference in average metallicity increases with decreasing mass, and reaches approximately 0.5 dex at $M_* = 10^{10} M_{\odot}$. Here, we revisit the MZ relation using a sample four times larger than presented in Zahid et al. (2014b). In particular, the number of massive ($M_* > 10^{11} M_{\odot}$) galaxies in the sample is larger by an order-of-magnitude.

8.1. Empirical metallicity determination using $[\text{NII}]/\text{H}\alpha$

We use the line ratio $[\text{NII}]/\text{H}\alpha$ to evaluate the gas-phase metallicity, i.e., the oxygen abundance normalized by 10^{12} hydrogen atoms, $12 + \log(\text{O}/\text{H})$. The advantage of using this ratio is the close spectral proximity of the lines thus not requiring any correction for extinction. The high-resolution mode of FMOS cleanly separates the two lines. The line ratio is converted to metallicity as given in Maiolino et al. (2008):

$$N2 = -0.7732 + 1.2357x - 0.2811x^2 - 0.7201x^3 - 0.3330x^4 \quad (6)$$

where $N2 = \log([\text{NII}]\lambda 6584/\text{H}\alpha)$ and $x = 12 + \log(\text{O}/\text{H}) - 8.69$. This relation is nearly linear over the metallicity range of interest ($8 < \log(\text{O}/\text{H}) < 9$), while at higher metallicity (above $N2 \sim -0.3$) the line ratio begins to saturate (Maiolino et al. 2008). This saturation is the result of metal cooling, which leads to a decrease in the collisional excitation rate of N^+ (Osterbrock & Ferland 2006).

Figure 13a shows the $[\text{NII}]\lambda 6584/\text{H}\alpha$ ratio as a function of stellar mass. We plot 436 galaxies with $\text{H}\alpha$ and $[\text{NII}]$ detections in Sample-1. The FMOS sample has a broad distribution of $[\text{NII}]/\text{H}\alpha$ that spans much of the SDSS locus (see also Zahid et al. 2014b). Many galaxies with less secure measurements ($1.5 < S/N([\text{NII}]) < 3$) have a low $[\text{NII}]/\text{H}\alpha$ ratio. This is expected because the intensity of the $[\text{NII}]$ line is generally much weaker than $\text{H}\alpha$ and difficult to detect with FMOS for a reasonable amount (\sim a few hours) of integration time. It is also shown that many galaxies have a high $[\text{NII}]/\text{H}\alpha$ ratio ranging from $N2 \sim -0.2$ to 0.2. The locus of such a population shows good agreement with the distribution of the local AGN-population and the bulk of the X-ray detected sources match the high $N2$ galaxies. This possibly suggests that AGNs are presented in our sample if there is no prior exclusion, especially, at high stellar masses (Mancini et al. 2015).

To overcome the low S/N of individual detections of the $[\text{NII}]$ line, we plot, in Figure 13b, the metallicities based on

²² <http://cstack.ucsd.edu/cstack/>

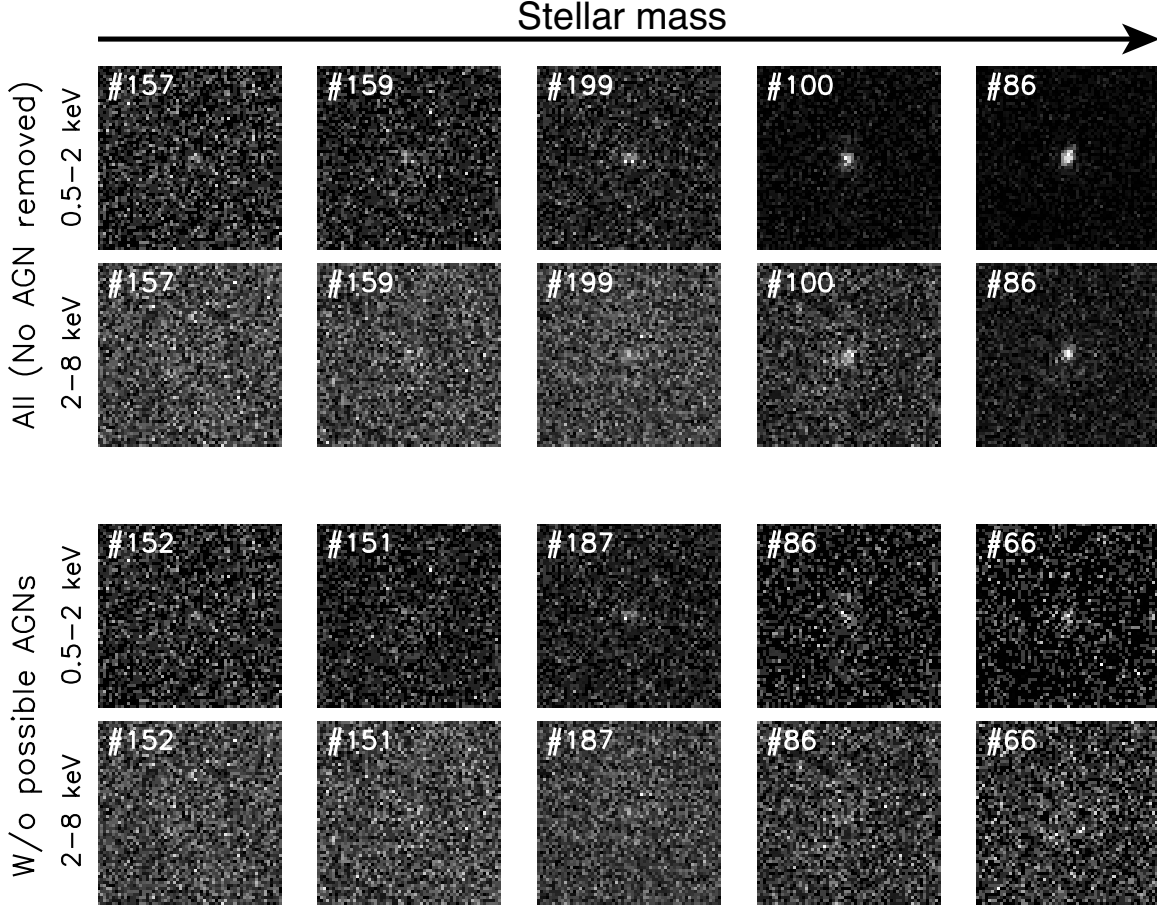


FIG. 11.— Chandra stacked images (30 arcsec on each side) in two bandpasses (soft: 0.5–2 keV, hard: 2–8 keV) of our sample in five bins of stellar mass. The number of individual images for stacking is indicated in each panel. The upper group shows the stacked images for the sample including all SED-selected galaxies without any removal of possible AGNs (case 1) in each stellar mass bin. The lower group shows for the sample in which all AGN candidates are removed (case 3) for the same stellar mass ranges as above. The stellar mass increases from left to right (see Table 3).

TABLE 3
X-RAY LUMINOSITY MEASUREMENTS

Median $\log M_*/M_\odot$ ^a Range	9.93 [9.1:10.1]	10.26 [10.1:10.4]	10.60 [10.4:10.8]	10.96 [10.8:11.1]	11.25 [11.1:11.7]
Case 1: No AGN exclusion applied					
No. of images ^b	157	159	199	100	86
Soft ^c	0.114 ± 0.079	0.321 ± 0.086	0.281 ± 0.077	1.199 ± 0.132	2.462 ± 0.180
Hard ^d	$< 0.748^f$	0.582 ± 0.504	0.825 ± 0.443	3.261 ± 0.664	7.252 ± 0.803
Full ^e	< 0.758	0.902 ± 0.511	1.106 ± 0.450	4.460 ± 0.677	9.714 ± 0.823
Case 2: X-ray luminous objects removed					
No. of images	157	156	195	93	78
Soft	0.114 ± 0.079	0.236 ± 0.086	0.230 ± 0.076	0.424 ± 0.115	0.484 ± 0.134
Hard	< 0.748	< 0.759	0.740 ± 0.443	1.572 ± 0.657	3.431 ± 0.776
Full	< 0.758	0.613 ± 0.513	0.970 ± 0.449	1.997 ± 0.667	3.916 ± 0.788
Case 3: All possible AGNs removed					
No. of images	152	151	187	86	66
Soft	< 0.121	0.214 ± 0.086	0.201 ± 0.078	0.452 ± 0.122	0.497 ± 0.145
Hard	< 0.767	< 0.774	0.832 ± 0.453	1.480 ± 0.681	2.872 ± 0.840
Full	< 0.776	< 0.785	1.034 ± 0.459	1.932 ± 0.692	3.369 ± 0.852

^a Median stellar mass each bin.

^b Number of stacked images in each bin.

^c Soft band (0.5–2 keV) luminosity in units of 10^{42} erg s^{-1} .

^d Hard band (2–8 keV) luminosity in units of 10^{42} erg s^{-1} .

^e Full band (0.5–8 keV) luminosity in units of 10^{42} erg s^{-1} .

^f Upper limit is given as 1.5 times of noise levels if $S/N < 1$.

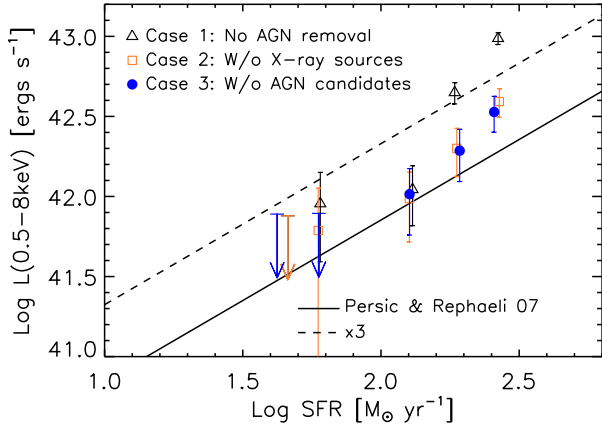


FIG. 12.— Comparison between the mean SFR (from dust-corrected $H\alpha$ luminosity) and the 0.5–8 keV luminosity $L_{0.5-8 \text{ keV}}$ in each bin of stellar mass. The X-ray luminosities $L_{0.5-8 \text{ keV}}$ are measured by stacking the Chandra ACIS-I images. Different symbols show the measurements for different cases of the AGN removal (triangles; no AGN removed, squares: without Chandra X-ray detected sources, filled circles: without all potential AGN candidates; see the text). An $SFR-L_X$ relation for star-forming galaxies from Persic & Rephaeli (2007) and a relation with three times larger $L_{0.5-8 \text{ keV}}$ are shown by the solid and dashed lines, respectively.

the average $[NII]/H\alpha$ ratios measured from the stacked spectra for Sample-1 split into eight bins of stellar mass (see Table 2). Average spectra reduce the bias with respect to detecting $[NII]$ since galaxies are only identified by the presence of an $H\alpha$ detection. As described in Section 3.3, we remove galaxies identified as AGN based on the BPT diagram (or $N2 > -0.1$ if no $[OIII]/H\beta$ measurement is available), X-ray detection, or $FWHM > 1000 \text{ km/s}$. For the local galaxies, we take the median $[NII]/H\alpha$ ratios in 50 bins of stellar mass, shown by squares with the 16 and 84 percentiles of the metallicity.

Our data show a level of metallicity similar to local galaxies at the massive end ($M_* > 10^{11} M_\odot$), while the average measurements in less massive galaxies are lower than those in local galaxies. The difference in metallicity with the local sample extends down to our lower mass limit ($\sim 10^{9.6} M_\odot$). The average $[NII]/H\alpha$ measurements are consistent with the previous measurements from Zahid et al. (2014b, gray triangles in Figure 13b). We further assess the effects of excluding potential AGN by their $[NII]/H\alpha$, particularly at the massive end. With an upper limit of -0.3 on individual values of $\log([NII]/H\alpha)$, the stacked measurements are still consistent with local massive galaxies, although the values are lower by $\Delta \log(O/H) \sim 0.15$.

In Figure 13b, we also show MZ relations based on $[NII]/H\alpha$ from the literature at $z \sim 1.4-2.3$ (Erb et al. 2006; Yabe et al. 2014, 2015; Steidel et al. 2014), which are converted here to Salpeter IMF and the Maiolino et al. (2008) calibration. Our measurements are nearly in agreement with the measurements by Yabe et al. (2014) also based on FMOS observations.

8.2. New calibration with $[NII]/[SII]$

Recently, Dopita et al. (2016) have introduced a new metallicity calibration using both the line ratios $[NII]/H\alpha$ and $[NII]/[SII]$. This calibration is almost independent of the ionization parameter and gas pressure, effective over the metal-

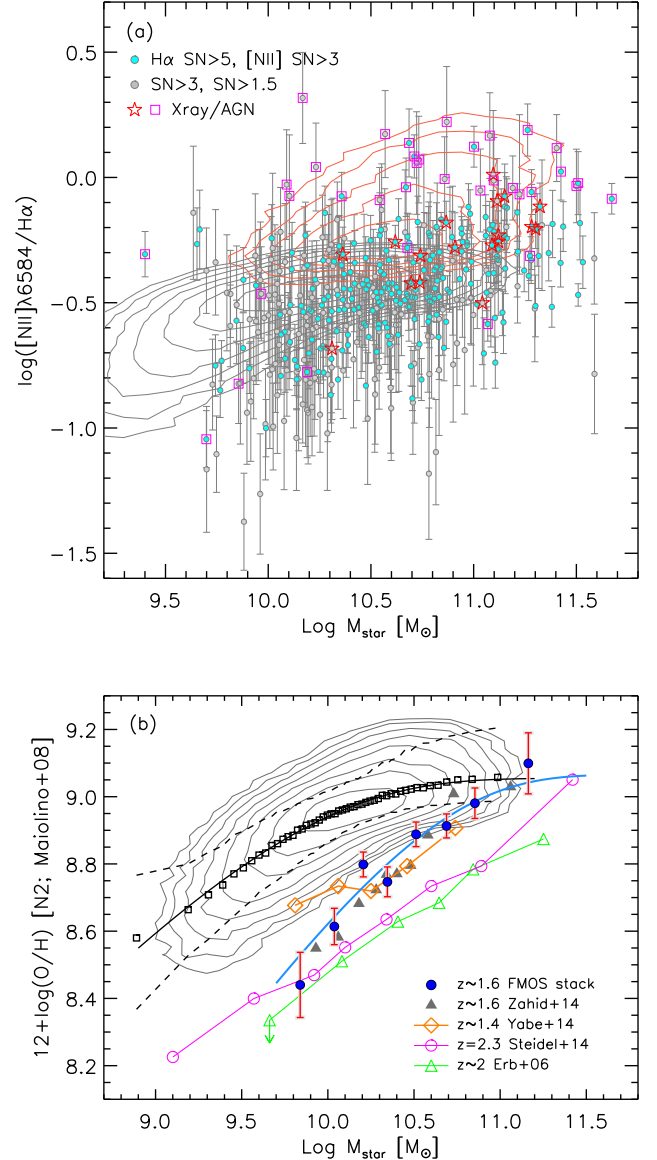


FIG. 13.— Mass-metallicity relation; *Panel (a)*: $[NII]/H\alpha$ as a function of stellar mass. Individual FMOS galaxies are shown with the quality of measurement as labelled (cyan, $S/N > 3$ for $H\alpha$ and $[NII]$ lines; gray, $S/N(H\alpha) > 3$ and $1.5 < S/N([NII]) < 3$). AGN candidates are highlighted by stars (X-ray detected sources) and magenta squares (others). Contours show the distribution of the local star-forming galaxies (gray) and AGNs (red). *Panel (b)*: Mass-metallicity relation. The oxygen abundance is calculated from the average $[NII]/H\alpha$ ratio with Equation 6. The $[NII]/H\alpha$ ratios of Sample-1 are measured based on the stacked spectra in eight mass bins (filled circles). Filled triangles indicate our previous measurement from Zahid et al. (2014b). Empty symbols show the measurements in the literature as labelled. Open squares show the median values for local galaxies divided in 50 stellar mass bins and dashed lines indicate the 68 percentile of the local SDSS galaxies. Solid curves show the best-fit relations parametrized in Equation 8, for the FMOS (blue) and the local (black) samples.

licity range of $8 < 12 + \log(O/H) < 9$, expressed as follows:

$$12 + \log(O/H) = 8.77 + N2S2 + 0.264N2 \quad (7)$$

where $N2S2$ is defined as Equation 5. The inclusion of the $[NII]/[SII]$ term in the determination of the metallicity provides an assessment of how nucleosynthesis has proceeded through the ratio of secondary-to-primary elements. This cal-

ibration assumes a relation between the N/O (\approx N/S) ratio and the O/H ratio. The authors argue that the offset in the BPT diagram of high- z galaxies relative to local galaxies can be explained by changes in the ionization parameter and gas pressure, without resorting to an explanation based on differences in the N/O vs. O/H relation as advocated by Masters et al. (2014) and Shapley et al. (2015). However, this rests on the assumption of a universal N/O vs. O/H relation, as illustrated in Figure 1 of Dopita et al. (2016), while it is not ensured for high- z galaxies. Indeed, the chemical evolutionary stage of high redshift galaxies, specifically concerning nitrogen enrichment, is unlikely to be the same as in local galaxies. Moreover, fluctuations in the gas content of galaxies in response to high accretion rates, would affect O/H but not the N/O or the N/S ratios. From the coefficients in Equation 7, the resulting oxygen abundance is far more sensitive to the N/S ratio than to the absolute abundance of nitrogen, indicating that the calibration is tightly linked to the specific chemical evolutionary stage of local galaxies. It is clear that a direct calibration of the relation between N/O and O/H is required to improve upon metallicity determinations of high-redshift galaxies.

With this caveat in mind, we present in Figure 14 the MZ relation with metallicity determined from Equation 7 for both local and our high- z galaxies. Similar to the [NII]/[SII] ratio shown in Figure 9a, the metallicity in local star-forming galaxies is nearly constant at low masses ($M_* \lesssim 10^{9.2} M_\odot$), where primary nitrogen production is dominant. We find a MZ relation for the FMOS sample essentially equivalent to the results based on the [NII]/H α ratio (shown in Figure 13b): the metallicities of high- z galaxies are, on average, smaller than those in local galaxies at low masses, then increase with increasing stellar mass, reaching a level ($12 + \log(\text{O}/\text{H}) \approx 8.9$) similar to local galaxies at $M_* \gtrsim 10^{11} M_\odot$. However, note that the metallicity range spanned by our sample ($8 \lesssim 12 + \log(\text{O}/\text{H}) \lesssim 8.9$) is slightly different from that in the case of the $N2$ -based metallicity with the Maiolino et al. (2008) calibration ($8.4 \lesssim 12 + \log(\text{O}/\text{H}) \lesssim 9.1$). We remind readers that there are likely systematic uncertainties in the absolute metallicity calibrations based on different techniques and/or indicators.

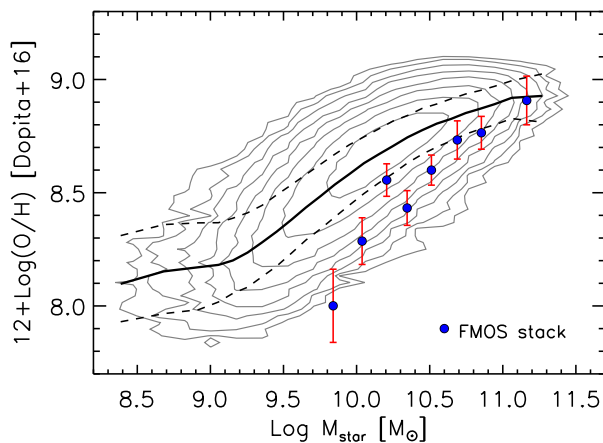


FIG. 14.— Mass–metallicity relation based on a calibration introduced by Dopita et al. (2016, Equation 7). Symbols are the same as those in Figure 13. Local galaxies are shown by contours with median value (solid line) and the 68% interval (dashed lines).

In this analysis, we remove those with $N2 > -0.1$ to exclude AGNs (see Section 3.3). However, there still remain the possibility that the average [NII]/H α measurements are enhanced by weak AGNs. Therefore, we examine if the metallicity measurements are affected by the changes in selecting which galaxies to stack. We lower the threshold to $N2 = -0.3$ thus excluding all galaxies with values above this limit. We find that galaxies at the high mass end still have metallicities in agreement with local massive galaxies. Therefore, we conclude that the most massive galaxies are fully matured, as reported when using the [NII]/H α -based metallicity.

8.3. Evolution of the MZ relation

We model the observed MZ relation based on the [NII]/H α ratios of our FMOS sample with a functional form implemented in Zahid et al. (2014a), which is parametrized as

$$12 + \log(\text{O}/\text{H}) = Z_0 + \log \left[1 - \exp \left(- \left[\frac{M_*}{M_0} \right]^\gamma \right) \right]. \quad (8)$$

Here, Z_0 is the asymptotic metallicity at the massive end. M_0 is the characteristic stellar mass where the relation begins to flatten, and γ is the power-law slope of the relation at $M_* \ll M_0$. This fitting function differs from the function used in our previous study (Zahid et al. 2014b) and has a more physically motivated form. We find consistent results for the current and previous measurements by fitting the MZ relation with the model given in Zahid et al. (2014b). Throughout the remainder of the discussion, we use Equation 8 to fit our data because it has the advantage that the parameters are physically interpretable (see Zahid et al. 2014a for details). The fit to the local MZ relation is derived using the same function and the median values in 50 stellar mass bins. The best-fit parameters are listed in Table 4. Our derivation at $z \sim 1.6$ is in agreement with an earlier version by Zahid et al. (2014a) accounting for the different methods to measure stellar mass and metallicity between the two studies.

In Figure 13b, the model well represents the observed MZ relations at $z \sim 0$ and $z \sim 1.6$. Z_0 and γ are statistically consistent between the two samples. Therefore, the evolution of the MZ relation is quantified by the evolution of the turnover mass M_0 at which the metallicity begins to saturate. Motivated by this fact, we fit a model to our data with Z_0 and γ fixed to the local values ($Z_0 = 9.055$ and $\gamma = 0.538$; see Table 4). In this case, we find M_0 to be consistent with the case where Z_0 and γ are free parameters.

Zahid et al. (2014a) introduced the concept of a universal relation between metallicity and the stellar-to-gas mass ratio (M_*/M_{gas}) as the underlying origin of the MZ relation. In this framework, $(M_*/M_0)^\gamma \sim (M_*/M_{\text{gas}})$ and the decline of M_0 with cosmic time is interpreted as a result of the decline of gas content. Figure 15 shows the relation between metallicity (from the [NII]/H α ratio) and $\gamma \log(M_*/M_0)$ for the local sample ($\gamma = 0.54$) and the FMOS sample ($\gamma = 0.71$, filled circles; $\gamma = 0.54$, open circles). The measurements from our sample agree well with the local relation, strongly supporting the existence of the universal relation since $z \sim 1.6$ to the present day. In this model, the slope of the MZ relation at $M_* < M_0$ is prescribed by the slope of the relation between stellar mass and gas mass (δ ; $M_{\text{gas}} \propto M_*^\delta$) as $\gamma = 1 - \delta$. Therefore, our result is consistent with that the slope of the M_* - M_{gas} relation has not significantly changed since $z \sim 1.6$.

We further explore the possibility that the slope γ evolves with cosmic time in contrast to the argument that the evolu-

TABLE 4
BEST-FIT PARAMETERS OF THE MASS–METALLICITY RELATION

Sample	Redshift ^a	Z_0	$\log(M_0/M_\odot)$	γ
SDSS	0.069	9.055 ± 0.003	9.69 ± 0.01	0.538 ± 0.008
FMOS	1.55	9.07 ± 0.13	10.5 ± 0.4	0.71 ± 0.25
FMOS	1.55	[9.055] ^b	10.51 ± 0.06	[0.538]

^a Median redshift of each sample.

^b Fixed values are given as [x].

ing MZ relation is explained only by a change in the turnover mass M_0 . There does appear to be evidence for a steeper slope of the MZ relation at high redshift. Setting γ as an extra free parameter reduces the best-fitting χ^2 by 3.2 as compared to the case with the fixed γ and Z_0 . In Figure 15, the fit with a free γ (filled circles) are in better agreement with the local relation than the fit with a γ fixed to the local value (0.54; open circles). In this context, the steeper slope of the MZ relation at $z \sim 1.6$ means that the slope of the M_*-M_{gas} relation is shallower (i.e., smaller δ) at $z \sim 1.6$ than at $z \sim 0$. If it is real, such an evolving slope can be interpreted as a result of the transition of stellar mass, at which the stored gas is effectively consumed, towards a lower mass scale with time.

However, selection effects may be present at low masses that impact our determination of γ . Our sample is potentially biased towards a population having high SFRs and being less obscured by dust. This bias may be induced by the observational limit of detecting $H\alpha$ and the self-imposed selection on the predicted $H\alpha$ flux. Metallicity is expected to be anti-correlated with SFR (see Section 8.4) and the amount of metal is commonly known to be correlated with the amount of dust (e.g., Issa et al. 1990; Schmidt & Boller 1993; Lisenfeld & Ferrara 1998). Therefore, such a selection may impact the shape of the MZ relation. In particular, the effects may be considerable at low masses because low mass dusty galaxies, which are expected to have a low $H\alpha$ flux and to be more metal rich, tend to fall below our selection limit. In such cases, the measurements at the lower mass end may be biased towards lower metallicities, leading to a MZ relation with a steeper slope.

In Figure 13b, the MZ relations derived at higher redshifts ($z \gtrsim 2$, Erb et al. 2006; Steidel et al. 2014) show a clear correlation between stellar mass and metallicity. At the lowest mass ($M_* \sim 10^{9.8} M_\odot$), our sample is in agreement with the relations at $z \gtrsim 2$. In contrast, our sample galaxies are more enriched as compared to $z \gtrsim 2$ galaxies at $M_* \gtrsim 10^{10} M_\odot$. The slope of the Steidel et al. MZ relation is found to be approximately 0.34, which is significantly shallower than those found in the relations at lower redshifts. However, the origin of the difference in the shape of the MZ relation is not clear. In contrast to Erb et al. (2006) and Steidel et al. (2014), Wuyts et al. (2014) reported that the shape of the MZ relation does not change up to $z \sim 2.3$ using a compilation of samples. As mentioned above, selection effects probably impact the shape of the MZ relation. In particular, there is the possibility that the $z \gtrsim 2$ samples that are shown in Figure 13 miss some of the dusty galaxies, which tend to be metal rich, because of their UV-based selection (Erb et al. 2006; Steidel et al. 2014).

8.4. Stellar mass–metallicity–SFR relation

An anti-correlation between metallicity and SFR at a fixed stellar mass has been seen in local galaxies (e.g., Ellison et al. 2008). A lower metallicity for galaxies with a high SFR

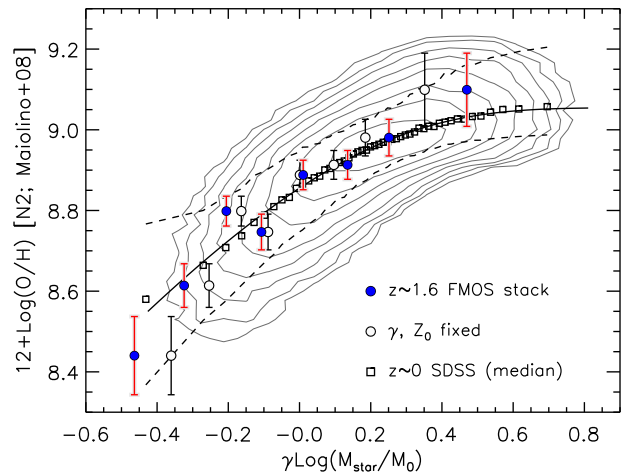


FIG. 15.— Metallicity vs. $\gamma \log(M_*/M_\odot)$ for the local and FMOS samples. Filled circles indicate the average metallicity based on the Sample-1 co-added spectra in eight mass bins (same as in Figure 13b). Open circles show our measurements with Z_0 and γ fixed to the local values. A solid curve is given by Equation 8 with the parameters that are determined from the SDSS sample. Dashed lines indicate the 68 percentiles.

may indicate that inflowing pristine (or metal-poor) gas decreases the oxygen abundance and enhances star formation. Mannucci et al. (2010) introduced SFR into the MZ relation as the third parameter, and proposed a relation between those three quantities, referred to as the *Fundamental Metallicity Relation* (FMR). Although its actual shape has not been completely established yet due to the difference in sample selection from one study to another, a number of studies have found that introducing SFR as a second parameter reduces the scatter in the MZ relation (Lara-López et al. 2010b, 2013; Mannucci et al. 2011; Yates et al. 2012; Andrews & Martini 2013; Zahid et al. 2014b).

Beyond the local universe, the dependence of SFR of the MZ relation has not been established yet (see e.g., Wuyts et al. 2014; Zahid et al. 2014b; Yabe et al. 2014; Steidel et al. 2014; Guo et al. 2016). We previously reported that the metallicities of high SFR galaxies are systematically lower than the metallicities of low SFR galaxies, by using an sBzK-selected subset of the current data (Zahid et al. 2014b). With the current data, we examine again if the metallicity depends on SFR at a given stellar mass. However, we do not confirm our previous results, i.e., do not find a significant dependence of the MZ relation on SFR. While this contradiction is possibly due to the effects of sample selection, it is still desirable to further study this issue with a larger sample and accurate SFR estimation to constrain (possibly weak) correlation between metallicity and SFR.

Next, we examine the cosmic evolution of the relation between metallicity, stellar mass, and SFR. It is worth noting

that a lack of a significant SFR– Z correlation at a given single redshift (i.e., within a narrower SFR range) does not mean that there is a lack of the correlation over a wider SFR range with consideration of the redshift evolution of the main sequence. In the context of the FMR, the redshift evolution of the MZ relation is expressed as a shift on the surface of the M_* –SFR– Z space while these parameters varying with cosmic time. Mannucci et al. (2010) defined a quantity combining M_* and SFR as $\mu_\alpha = \log M_* - \alpha \log \text{SFR}$ that minimizes the dispersion in metallicity over small intervals on a grid of the M_* –SFR plane. Here, the parameter α refers to the projection parameter. We choose $\alpha = 0.32$ for comparison with the original FMR by Mannucci et al. (2010), although $\alpha = 0.30$ is derived for the $[\text{NII}]/\text{H}\alpha$ -based metallicity by Andrews & Martini (2013) and Zahid et al. (2014b) using the SDSS sample. The use of $\alpha = 0.30$ does not change our conclusions. We note that Mannucci et al. (2010) use the metallicity calibration of Maiolino et al. (2008), the same as implemented here, thus there is no need for an additional conversion factor.

Figure 16 shows the metallicity of the $z \sim 1.6$ galaxies in the FMOS sample derived from the $[\text{NII}]/\text{H}\alpha$ ratios as a function of the projected axis (μ) with the FMR from Mannucci et al. (2010) (thin solid curve) overlaid. The line ratios are measured on the composite spectra of Sample-1 in eight bins of either the μ value or stellar mass. In the latter case, the values of μ are calculated by median stellar mass and SFR in each bin. Here, we show the results obtained using $\text{H}\alpha$ -based SFRs; our conclusion does not change when using SED-based SFRs. The measurements in the two binning cases (μ_α -bin or M_* -bin) are consistent within the uncertainties.

Our FMOS sample shows good agreement with the Mannucci et al. FMR (thin solid curve in Figure 16) while there is a small offset towards higher metallicities at $\mu \sim 10$. However, we note that Mannucci et al. (2010) derived the FMR using *aperture-based* SFR, which is not corrected for the fiber aperture loss, while we derive the *total* SFRs for our FMOS sample accounting for the fiber loss (see Zahid et al. 2014b, for further discussion). The use of a mixture of total and aperture-based SFRs may be misleading and result in an inaccurate physical understanding. Therefore, we derive a new relation between μ and metallicity for the local galaxies, using total SFRs based on $\text{H}\alpha$ luminosities, for which the aperture effect and dust extinction are corrected. Figure 16 shows the distribution and the average relation, based on median metallicity in 40 bins of μ , of the local sample (contours and thick solid line). Our high-redshift measurements are in good agreement with the local galaxies at $\mu > 9.8$. In contrast, the difference in metallicity with the local relation extends at $\mu < 9.8$ down to the lower limit, although the discrepancy becomes smaller as compared with the offset in the MZ relation. At the low mass end, the offset is approximately $\Delta \log(\text{O}/\text{H}) \sim 0.2$ dex in the FMR while about 0.3 dex in the MZ relation. Here, we stress that there still remain a significant offset in the metallicity between the relations at two epochs in spite of the fact that the bias towards high SFRs in our sample is mitigated by computing the projection axis μ . Thus, as first reported in Zahid et al. (2014b), our data do not support the extrapolation from the local galaxies, particularly at low M_* and high SFR, as proposed by Mannucci et al. (2010).

Maier et al. (2014) have studied the FMR at $z > 2$ and found that high- z galaxies in their sample are consistent with a universal FMR that is based on the physically motivated formu-

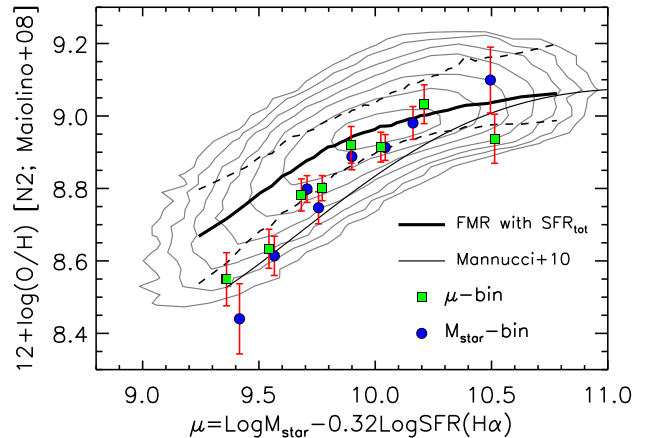


FIG. 16.— Metallicity versus $\mu_{\alpha=0.32}(M_*, \text{SFR})$. The metallicities are determined from the $[\text{NII}]/\text{H}\alpha$ ratio and μ is calculated using $\text{H}\alpha$ -based SFRs for both the local sample and our FMOS sample. Symbols indicate the measurements on the stacked spectra in eight bins of either stellar mass (blue filled circles) or μ value (green filled squares). Contours show distribution of the local star-forming galaxies, with the median (FMR with total SFR; thick solid line) and the central 68 percentiles (dotted lines). A thin solid line indicates the original FMR derived by Mannucci et al. (2010) (based on aperture SFRs).

lation from Lilly et al. (2013) (see also Onodera et al. 2016), but not with the Mannucci et al. FMR. In the framework of Lilly et al. (2013), the equilibrium gas-phase metallicity, Z_{eq} , is given as a function of M_* and SFR. We follow the parametrization of Equation 3 in Maier et al. (2014):

$$Z_{\text{eq}} = Z_{\text{in}} + \frac{y}{1 + \lambda(1-R)^{-1} + \varepsilon^{-1}((1+\beta-b)\text{SFR}/M_* - 0.15)} \quad (9)$$

where Z_{in} is the metallicity of the infalling gas, y is the yield, $R \approx 0.4$ is the fraction of mass returned into ISM, λ is the mass-loading factor, given as $\lambda \propto M_*^a$, and $\varepsilon = \text{SFR}/M_{\text{gas}} \propto M_*^b$ is the star formation efficiency. $\beta \approx -0.1$ is the slope of the M_* -sSFR relation, i.e., $\text{sSFR} \propto M_*^\beta$. We note that Equation 9 is a form for $z = 0$ and that the form for high redshifts will depend on the time variation of parameters, as discussed in Lilly et al. (2013). In particular, the star formation efficiency is likely to increase with redshift by a factor $\sim (1+z)$ (e.g., Genzel et al. 2010; Sargent et al. 2014). Here, we compare our measurements at $z \sim 1.6$ to this model without considering the time dependence to examine whether our measurement at $z \sim 1.6$ follow a non-evolving Z – M_* –SFR relation.

We determine the parameters from a model fit to the SDSS sample using total SFRs, as listed in Table 5. The derived values are nearly equivalent to those given in Lilly et al. (2013) except for the star formation efficiency ε that is two or three times higher here. This is most likely because we use the total SFRs to derive the FMR of the SDSS sample whereas Lilly et al. (2013) use aperture-based SFRs, as in Mannucci et al. (2010). In the fitting, Z_{in} is fixed to zero while the use of a different value within $0 < Z_{\text{in}}/y < 0.1$ does not change our conclusions.

Based on this physically-motivated model, we find that our sample at $z \sim 1.6$ is consistent with a non-evolving FMR relation. Figure 17 shows median metallicities for galaxies in our sample and for local objects, as a function of SFR (panel a) and sSFR (panel b) for galaxies of different M_* . We first

separate the local sources into 0.2 dex-wide M_* bins, then divide into 50 SFR bins within each M_* bin. The median metallicities are shown separately for each M_* bin, as color-coded in the plot. The functional form of the FMR (Lilly et al. 2013) reproduces the behavior of local galaxies in each mass bin (dashed curves). Filled circles show the average metallicities of the FMOS galaxies (Sample-1) based on the composite spectra in eight mass bins. Figure 17 shows good agreement between our $z \sim 1.6$ measurements and the model prediction extrapolated from the local sample within ~ 0.1 dex at each M_* . This is more clearly seen in the lower panels *d* and *e*, in which we show the deviations of observed metallicity from the model values at corresponding M_* and SFR.

The agreement between our observations and the model is also seen in panels *c* and *f* of Figure 17, where we present the MZ relation and the metallicity deviation from the model for the local (open squares) and FMOS galaxies (filled circles), respectively. To compute median metallicities for local galaxies, we separate the sample into 0.4 dex-wide SFR bins, then divide into 50 M_* bins. The median metallicities are presented as a function of M_* separately for each SFR bin as color-coded. We overlaid the predictions from the fitted FMR at median SFR of each bin for the SDSS (dashed lines) and our FMOS (solid lines) samples. The expected metallicities at the median M_* and SFR of each bin of the FMOS sample (open diamonds) show good agreement with the data points.

Our measurements at low masses require a rapid decline of metallicity at higher SFRs (see Figure 17*ab*). This trend is naturally induced by considering galaxy evolution regulated by gas inflow and mass loss in the model of Lilly et al. (2013). Our finding is consistent with the conclusion in Maier et al. (2014), claiming that whether a FMR is truly fundamental (i.e., independent of redshift) depends on the formulation of the model and its extrapolation to regions of the M_* -SFR parameter space different from that occupied by local galaxies.

Finally, we note that the deviation from the model at $z \sim 1.6$ likely to be correlated with stellar mass (or SFR) and, in particular, the deviation at high masses ($M_* \gtrsim 10^{10.5} M_\odot$) is statistically significant. In this study, we do not take account for the time evolution of model parameters. However, in reality, the parameters are possibly dependent on the epoch, although their time dependence has not been established yet. We find that it is difficult to reproduce the observed $z \sim 1.6$ MZ relation unless assuming a much higher mass loading factor (twice or more locally). However, we need a larger sample that spans wide range of the parameter space with redshift, stellar mass, and SFR, to obtain further physical insights over cosmic time.

9. CONCLUSIONS

We investigate the physical conditions of HII regions in star-forming galaxies on the main sequence at $1.43 < z < 1.74$ using the FMOS-COSMOS survey. This is the first time to probe such a large sample over a wide stellar mass range of $10^{9.6} \lesssim M_*/M_\odot \lesssim 10^{11.6}$ at these redshifts. Our main results are as follows:

1. We confirm a clear offset from the mean locus of the local star-forming galaxies on the BPT diagram using both individual measurements and stacking measurements for our FMOS sources. This offset amounts to an increase by a factor of ~ 0.5 dex in the mass-excitation (MEx) diagram ([OIII]/H β vs. M_*) between our FMOS sample and local SDSS galaxies.

2. We assess the effects of AGNs on our stacking analysis by using the X-ray imaging data set from the *Chandra*-COSMOS Legacy survey. Stacking the images permit us to evaluate the average X-ray luminosity and the contribution from AGNs in subsamples separated into stellar mass bins. We make sure that the AGN contamination is well removed, by excluding objects that are included in the X-ray point source catalog and those identified based on their rest-frame optical emission line properties, thus not responsible for the offsets seen in the BPT and MEx diagrams.
3. We measure the emission line ratio [SII] $\lambda\lambda 6717, 6731$ /H α with average spectra and find lower values of [SII]/H α as compared with local star-forming galaxies at a fixed [OIII]/H β (see Figure 6 in Section 5.2). These smaller [SII]/H α ratios suggest that a higher ionization parameter of the ISM is evident as opposed to a harder ionizing radiation field.
4. The average electron density is measured based on the emission line ratio [SII] $\lambda 6717$ /[SII] $\lambda 6731$ using stacked spectra that gives a value of $n_e = 222_{-128}^{+172} \text{ cm}^{-3}$ for the full sample, which is higher than the average of local star-forming galaxies ($\approx 10\text{--}10^2 \text{ cm}^{-3}$). This enhancement in electron density is consistent with those shown in a selected local sample with high star formation rates: such an enhancement may contribute to offsets seen in the BPT and MEx diagrams.
5. A relatively high ionization parameter in galaxies at $z \sim 1.6$ is supported by a recently-proposed emission line diagnostic (see Figure 10), which indicates that galaxies in our FMOS sample have an average ionization parameter $\log U \sim -3.3\text{--}3.2$, approximately 0.3 dex higher than the average of local star-forming galaxies ($\log U \sim -3.5$). With a relatively high electron density, a high ionization parameter expects to require a sufficient enhancement of the production rate of ionizing photons in each HII gas cloud. Such an enhancement of the ionizing photon flux is likely caused by a scaling up of the radiation field rather than a hardening of its spectrum.
6. The measurements of the line ratio [NII]/[SII] indicate that the secondary production of nitrogen is predominant in star-forming galaxies above $M_* \gtrsim 10^{10} M_\odot$ at $z \sim 1.6$. In contrast, it is likely that in lower mass galaxies ($M_* \lesssim 10^{10} M_\odot$), the primary process still dominate the nitrogen production. Furthermore, we find that our sample has higher [NII]/[SII] ratios relative to the level of [OIII]/H β , as compared to local galaxies. This may indicate that galaxies in our sample have higher excitation state relative to their evolutionary stage of the chemical enrichment.
7. We derive the mass-metallicity relation from the [NII]/H α ratio for our $z \sim 1.6$ sample, using the calibration of Maiolino et al. (2008). Our results are fully consistent with the previous derivation for a sBzK-selected sample in the FMOS-COSMOS survey (Zahid et al. 2014b). The current data strengthens our previous result that the most massive galaxies ($M_* \gtrsim 10^{11} M_\odot$) are fully matured at a level similar to local galaxies.

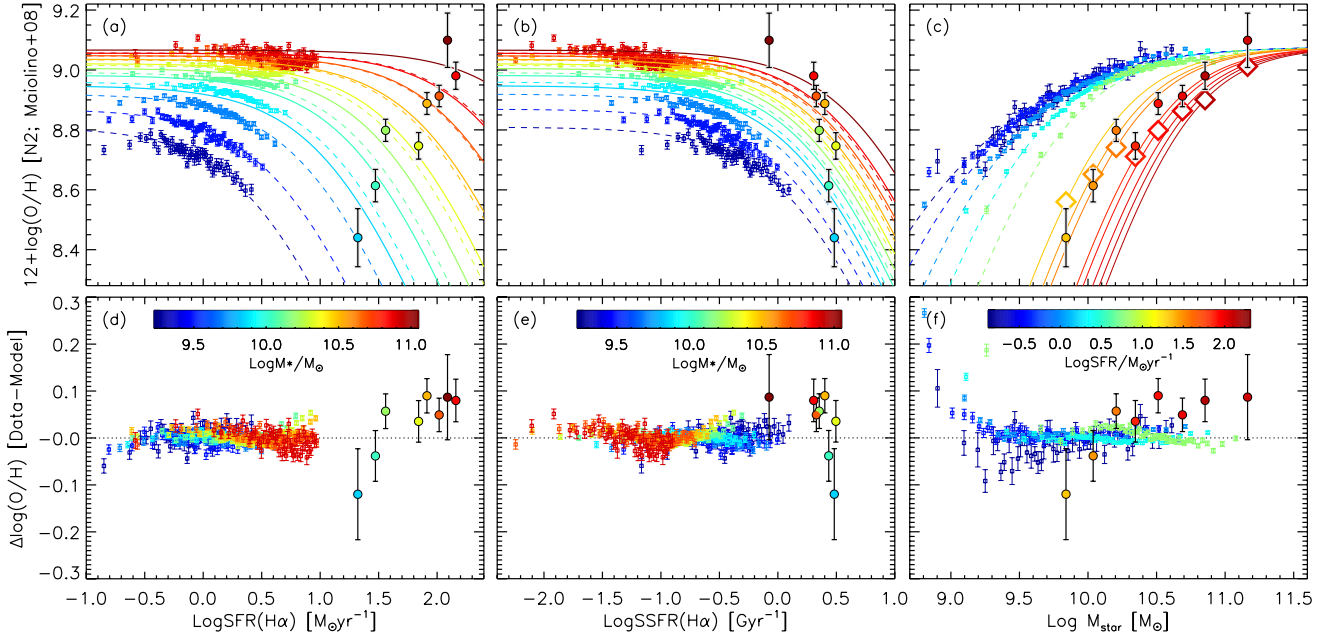


FIG. 17.— Metallicity as a function of SFR (*Panel a*), sSFR (*b*) and stellar mass (*c*) as compared to the model of Lilly et al. (2013). The FMOS measurements (Sample-1) based on composite spectra in eight mass bins are indicated by filled circles, color-coded by M_* (*panel a* and *b*) or SFR (*c*). Colored open squares show median metallicities of the SDSS galaxies. Dashed lines show the model metallicity computed for the SDSS sample from Equation 9 at median M_* (*a* and *b*) or SFR (*c*) in each bin for our FMOS sample. In *Panel c*, diamonds indicates the metallicities predicted by the best-fit FMR at the median M_* and SFR for each bin of our FMOS sample. *Panels d, e, f*: Differences between observed metallicities and theoretical predictions at the corresponding M_* and SFR from the model fit to the local sample (related to panels *a, b*, and *c*, respectively.)

TABLE 5
FIT OF LILLY ET AL. (2013) FMR MODEL TO THE SDSS SAMPLE

$\log y^a$	λ_{10}^b	a	ε_{10}^{-1} [Gyr] ^c	b
9.08 ± 0.02	0.27 ± 0.04	-0.64 ± 0.05	1.2 ± 0.2	0.45 ± 0.07

^a Yield parameter given in units of $12 + \log(\text{O}/\text{H})$

^b Mass-loading factor at $M_* = 10^{10} M_\odot$.

^c Star formation efficiency at $M_* = 10^{10} M_\odot$.

In contrast, at the least massive end ($M_* \sim 10^{9.8} M_\odot$), the metallicity is on average ~ 0.4 dex smaller than local galaxies. Our sample at $z \sim 1.6$ is in good agreement with a universal metallicity relation proposed by Zahid et al. (2014a), which is founded on the fundamental relation between metallicity and stellar-to-gas mass ratio.

8. We evaluate metallicity adopting a new calibration by Dopita et al. (2016), which uses the line ratios $[\text{NII}]/[\text{SII}]$ and $[\text{NII}]/\text{H}\alpha$. The derived mass–metallicity relation shows a trend that is qualitatively the same as the relation based on the $[\text{NII}]/\text{H}\alpha$ ratio, while the absolute values of metallicity is slightly different from those based on the $[\text{NII}]/\text{H}\alpha$ ratio.
9. The mass–metallicity–SFR relation for our FMOS sample shows a discrepancy from the FMR derived by Mannucci et al. (2010), with metallicities smaller than values expected by the extrapolation from local galax-

ies. In contrast, our measurements are consistent with a physically-motivated model from Lilly et al. (2013), in which the star formation is instantaneously regulated by the gas mass, gas inflow, and mass loss by outflow. This model well reproduces a rapid decline in metallicity at high SFRs as shown in our data.

This paper is based on data collected at the Subaru Telescope, which is operate by the National Astronomical Observatory of Japan. We greatly thank the Subaru telescope staff (especially K. Aoki) for their great help in the observations. We would thank M. Fukugita for helpful discussions.

We appreciate the MPA/JHU team for making their catalog public. Funding for SDSS-III has been provided by the Alfred P. Sloan Foundation, the Participating Institutions, the National Science Foundation, and the U.S. Department of Energy Office of Science. The SDSS-III web site is <http://www.sdss3.org/>.

D.K. is supported through the Grant-in-Aid for JSPS Fellows (No. 26-3216).

REFERENCES

- Abazajian, K. N., Adelman-McCarthy, J. K., Agüeros, M. A., et al. 2009, *ApJS*, 182, 543
 Alam, S., Albareti, F. D., Allende Prieto, C., et al. 2015, *ApJS*, 219, 12
 Aller, L. H. 1942, *ApJ*, 95, 52
 Andrews, B. H., & Martini, P. 2013, *ApJ*, 765, 140
 Arnouts, S., & Ilbert, O. 2011, LePHARE: Photometric Analysis for Redshift Estimate, Astrophysics Source Code Library, ascl:1108.009
 Baldwin, J. A., Phillips, M. M., & Terlevich, R. 1981, *PASP*, 93, 5

- Bouché, N., Hohensee, W., Vargas, R., et al. 2012, *MNRAS*, 426, 801
- Brinchmann, J., Charlot, S., White, S. D. M., et al. 2004, *MNRAS*, 351, 1151
- Brinchmann, J., Pettini, M., & Charlot, S. 2008, *MNRAS*, 385, 769
- Brusa, M., Fiore, F., Santini, P., et al. 2009, *A&A*, 507, 1277
- Bruzual, G., & Charlot, S. 2003, *MNRAS*, 344, 1000
- Bundy, K., Georgakakis, A., Nandra, K., et al. 2008, *ApJ*, 681, 931
- Calzetti, D., Armus, L., Bohlin, R. C., et al. 2000, *ApJ*, 533, 682
- Chabrier, G. 2003, *PASP*, 115, 763
- Cid Fernandes, R., Stasińska, G., Schlickmann, M. S., et al. 2010, *MNRAS*, 403, 1036
- Civano, F., Marchesi, S., Comastri, A., et al. 2016, *ApJ*, 819, 62
- Copetti, M. V. F., Mallmann, J. A. H., Schmidt, A. A., & Castañeda, H. O. 2000, *A&A*, 357, 621
- Cresci, G., Mannucci, F., Maiolino, R., et al. 2010, *Nature*, 467, 811
- Daddi, E., Cimatti, A., Renzini, A., et al. 2004, *ApJ*, 617, 746
- Dalcanton, J. J. 2007, *ApJ*, 658, 941
- Dickey, J. M., & Lockman, F. J. 1990, *ARA&A*, 28, 215
- Dominguez, A., Siana, B., Henry, A. L., et al. 2013, *ApJ*, 763, 145
- Dopita, M. A., Kewley, L. J., Heisler, C. A., & Sutherland, R. S. 2000, *ApJ*, 542, 224
- Dopita, M. A., Kewley, L. J., Sutherland, R. S., & Nicholls, D. C. 2016, *Ap&SS*, 361, 61
- Dopita, M. A., Sutherland, R. S., Nicholls, D. C., Kewley, L. J., & Vogt, F. P. A. 2013, *ApJS*, 208, 10
- Elbaz, D., Daddi, E., Le Borgne, D., et al. 2007, *A&A*, 468, 33
- Ellison, S. L., Patton, D. R., Simard, L., & McConnachie, A. W. 2008, *ApJ*, 672, L107
- Elvis, M., Civano, F., Vignali, C., et al. 2009, *ApJS*, 184, 158
- Erb, D. 2008, in *Astronomical Society of the Pacific Conference Series*, Vol. 399, *Panoramic Views of Galaxy Formation and Evolution*, ed. T. Kodama, T. Yamada, & K. Aoki, 239
- Erb, D. K., Shapley, A. E., Pettini, M., et al. 2006, *ApJ*, 644, 813
- Evans, I. N., & Dopita, M. A. 1985, *ApJS*, 58, 125
- Finlator, K., & Davé, R. 2008, *MNRAS*, 385, 2181
- Genzel, R., Tacconi, L. J., Gracia-Carpio, J., et al. 2010, *MNRAS*, 407, 2091
- Groves, B., Brinchmann, J., & Walcher, C. J. 2012, *MNRAS*, 419, 1402
- Guo, R., Hao, C.-N., Xia, X.-Y., Wei, P., & Guo, X. 2016, *ArXiv e-prints*, arXiv:1603.04988
- Hayashi, M., Ly, C., Shimasaku, K., et al. 2015, *PASJ*, 67, 80
- Ilbert, O., Salvato, M., Le Floc'h, E., et al. 2010, *ApJ*, 709, 644
- Ilbert, O., McCracken, H. J., Le Fèvre, O., et al. 2013, *A&A*, 556, A55
- Issa, M. R., MacLaren, I., & Wolfendale, A. W. 1990, *A&A*, 236, 237
- Iwamuro, F., Moritani, Y., Yabe, K., et al. 2012, *PASJ*, 64, 59
- Juneau, S., Dickinson, M., Alexander, D. M., & Salim, S. 2011, *ApJ*, 736, 104
- Juneau, S., Bournaud, F., Charlot, S., et al. 2014, *ApJ*, 788, 88
- Kartaltepe, J. S., Sanders, D. B., Silverman, J. D., et al. 2015, *ApJ*, 806, L35
- Kashino, D., Silverman, J. D., Rodighiero, G., et al. 2013, *ApJ*, 777, L8
- Kauffmann, G., Heckman, T. M., White, S. D. M., et al. 2003a, *MNRAS*, 341, 33
- Kauffmann, G., Heckman, T. M., Tremonti, C., et al. 2003b, *MNRAS*, 346, 1055
- Kennicutt, Jr., R. C. 1998, *ARA&A*, 36, 189
- Kewley, L. J., & Dopita, M. A. 2002, *ApJS*, 142, 35
- Kewley, L. J., Dopita, M. A., Leitherer, C., et al. 2013a, *ApJ*, 774, 100
- Kewley, L. J., Groves, B., Kauffmann, G., & Heckman, T. 2006, *MNRAS*, 372, 961
- Kewley, L. J., Jansen, R. A., & Geller, M. J. 2005, *PASP*, 117, 227
- Kewley, L. J., Maier, C., Yabe, K., et al. 2013b, *ApJ*, 774, L10
- Kewley, L. J., Zahid, H. J., Geller, M. J., et al. 2015, *ApJ*, 812, L20
- Kimura, M., Maihara, T., Iwamuro, F., et al. 2010, *PASJ*, 62, 1135
- Köppen, J., & Edmunds, M. G. 1999, *MNRAS*, 306, 317
- Koyama, Y., Kodama, T., Hayashi, M., et al. 2015, *MNRAS*, 453, 879
- Kriek, M., Shapley, A. E., Reddy, N. A., et al. 2015, *ApJS*, 218, 15
- Kroupa, P. 2001, *MNRAS*, 322, 231
- Lamareille, F., Brinchmann, J., Contini, T., et al. 2009, *A&A*, 495, 53
- Lara-López, M. A., Bongiovanni, A., Cepa, J., et al. 2010a, *A&A*, 519, A31
- Lara-López, M. A., Cepa, J., Bongiovanni, A., et al. 2010b, *A&A*, 521, L53
- Lara-López, M. A., Hopkins, A. M., López-Sánchez, A. R., et al. 2013, *MNRAS*, 434, 451
- Lehmer, B. D., Brandt, W. N., Alexander, D. M., et al. 2008, *ApJ*, 681, 1163
- Levesque, E. M., Kewley, L. J., & Larson, K. L. 2010, *AJ*, 139, 712
- Lilly, S. J., Carollo, C. M., Pipino, A., Renzini, A., & Peng, Y. 2013, *ApJ*, 772, 119
- Lisenfeld, U., & Ferrara, A. 1998, *ApJ*, 496, 145
- Liu, X., Shapley, A. E., Coil, A. L., Brinchmann, J., & Ma, C.-P. 2008, *ApJ*, 678, 758
- Madau, P., & Dickinson, M. 2014, *ARA&A*, 52, 415
- Magdis, G. E., Daddi, E., Sargent, M., et al. 2012, *ApJ*, 758, L9
- Maier, C., Lilly, S. J., Ziegler, B. L., et al. 2014, *ApJ*, 792, 3
- Maiolino, R., Nagao, T., Grazian, A., et al. 2008, *A&A*, 488, 463
- Mancini, C., Renzini, A., Daddi, E., et al. 2015, *MNRAS*, 450, 763
- Mannucci, F., Cresci, G., Maiolino, R., Marconi, A., & Gnerucci, A. 2010, *MNRAS*, 408, 2115
- Mannucci, F., Salvaterra, R., & Campisi, M. A. 2011, *MNRAS*, 414, 1263
- Markwardt, C. B. 2009, in *Astronomical Society of the Pacific Conference Series*, Vol. 411, *Astronomical Data Analysis Software and Systems XVIII*, ed. D. A. Bohlender, D. Durand, & P. Dowler, 251
- Masters, D., McCarthy, P., Siana, B., et al. 2014, *ApJ*, 785, 153
- McCracken, H. J., Milvang-Jensen, B., Dunlop, J., et al. 2012, *A&A*, 544, A156
- Miyaji, T., Griffiths, R. E., & C-COSMOS Team. 2008, in *AAS/High Energy Astrophysics Division*, Vol. 10, *AAS/High Energy Astrophysics Division #10*, 4.01
- Nakajima, K., & Ouchi, M. 2014, *MNRAS*, 442, 900
- Nakamura, O., Fukugita, M., Brinkmann, J., & Schneider, D. P. 2004, *AJ*, 127, 2511
- Newman, S. F., Buschkamp, P., Genzel, R., et al. 2014, *ApJ*, 781, 21
- Onodera, M., Carollo, C. M., Lilly, S., et al. 2016, *ArXiv e-prints*, arXiv:1602.02779
- Osterbrock, D. E., & Ferland, G. J. 2006, *Astrophysics of gaseous nebulae and active galactic nuclei*
- Pagel, B. E. J., Edmunds, M. G., Blackwell, D. E., Chun, M. S., & Smith, G. 1979, *MNRAS*, 189, 95
- Pagel, B. E. J., Edmunds, M. G., & Smith, G. 1980, *MNRAS*, 193, 219
- Peeples, M. S., & Shankar, F. 2011, *MNRAS*, 417, 2962
- Pérez-Montero, E., & Contini, T. 2009, *MNRAS*, 398, 949
- Persic, M., & Rephaeli, Y. 2007, *A&A*, 463, 481
- Pilyugin, L. S., Vílchez, J. M., Mattsson, L., & Thuan, T. X. 2012, *MNRAS*, 421, 1624
- Price, S. H., Kriek, M., Brammer, G. B., et al. 2014, *ApJ*, 788, 86
- Reddy, N. A., Erb, D. K., Steidel, C. C., et al. 2005, *ApJ*, 633, 748
- Rudie, G. C., Steidel, C. C., Trainor, R. F., et al. 2012, *ApJ*, 750, 67
- Sabbadin, F., Minello, S., & Bianchini, A. 1977, *A&A*, 60, 147
- Salpeter, E. E. 1955, *ApJ*, 121, 161
- Sanders, R. L., Shapley, A. E., Kriek, M., et al. 2016, *ApJ*, 816, 23
- Sargent, M. T., Daddi, E., Béthermin, M., et al. 2014, *ApJ*, 793, 19
- Schmidt, K.-H., & Boller, T. 1993, *Astronomische Nachrichten*, 314, 361
- Scoville, N., Aussel, H., Sheth, K., et al. 2014, *ApJ*, 783, 84
- Shapley, A. E., Coil, A. L., Ma, C.-P., & Bundy, K. 2005, *ApJ*, 635, 1006
- Shapley, A. E., Reddy, N. A., Kriek, M., et al. 2015, *ApJ*, 801, 88
- Shimakawa, R., Kodama, T., Steidel, C. C., et al. 2015, *MNRAS*, 451, 1284
- Shirazi, M., Brinchmann, J., & Rahmati, A. 2014, *ApJ*, 787, 120
- Silverman, J. D., Lamareille, F., Maier, C., et al. 2009, *ApJ*, 696, 396
- Silverman, J. D., Kashino, D., Sanders, D., et al. 2015, *ApJS*, 220, 12
- Steidel, C. C., Rudie, G. C., Strom, A. L., et al. 2014, *ApJ*, 795, 165
- Stott, J. P., Sobral, D., Bower, R., et al. 2013, *MNRAS*, 436, 1130
- Tonegawa, M., Totani, T., Okada, H., et al. 2015, *PASJ*, 67, 81
- Tremonti, C. A., Heckman, T. M., Kauffmann, G., et al. 2004, *ApJ*, 613, 898
- Valentino, F., Daddi, E., Strazzullo, V., et al. 2015, *ApJ*, 801, 132
- van Zee, L., Salzer, J. J., Haynes, M. P., O'Donoghue, A. A., & Balonek, T. J. 1998, *AJ*, 116, 2805
- Veilleux, S., & Osterbrock, D. E. 1987, *ApJS*, 63, 295
- Whitaker, K. E., Franx, M., Leja, J., et al. 2014, *ApJ*, 795, 104
- Wink, J. E., Wilson, T. L., & Bieging, J. H. 1983, *A&A*, 127, 211
- Wuyts, E., Kurk, J., Förster Schreiber, N. M., et al. 2014, *ApJ*, 789, L40
- Yabe, K., Ohta, K., Iwamuro, F., et al. 2012, *PASJ*, 64, 60
- , 2014, *MNRAS*, 437, 3647
- Yabe, K., Ohta, K., Akiyama, M., et al. 2015, *PASJ*, 67, 102
- Yamada, T., Kajisawa, M., Akiyama, M., et al. 2009, *ApJ*, 699, 1354
- Yates, R. M., Kauffmann, G., & Guo, Q. 2012, *MNRAS*, 422, 215
- Zahid, H. J., Dima, G. I., Kudritzki, R.-P., et al. 2014a, *ApJ*, 791, 130
- Zahid, H. J., Kewley, L. J., & Bresolin, F. 2011, *ApJ*, 730, 137
- Zahid, H. J., Kashino, D., Silverman, J. D., et al. 2014b, *ApJ*, 792, 75